

# Enhanced shape recovery in advection–diffusion problems via a novel ADMM-based CCBM optimization

Elmehdi Cherrat<sup>\*,1</sup> · Lekbir Afraites<sup>\*,2</sup> · Julius Fergy Tiongson Rabago<sup>†</sup>

<sup>\*</sup>Mathematics and Interactions Teams (EMI)

Faculty of Sciences and Techniques

Sultan Moulay Slimane University

Beni Mellal, Morocco

<sup>1</sup>[cherrat.elmehdi@gmail.com](mailto:cherrat.elmehdi@gmail.com), <sup>2</sup>[l.afraites@usms.ma](mailto:l.afraites@usms.ma)

<sup>†</sup>Faculty of Mathematics and Physics

Institute of Science and Engineering

Kanazawa University, Kanazawa 920-1192, Japan

[jftrabago@gmail.com](mailto:jftrabago@gmail.com)

August 23, 2025

## Abstract

This work proposes a novel shape optimization framework for geometric inverse problems governed by the advection–diffusion equation, based on the coupled complex boundary method (CCBM). Building on recent developments [2, 45, 46, 47, 51], we aim to recover the shape of an unknown inclusion via shape optimization driven by a cost functional constructed from the imaginary part of the complex-valued state variable over the entire domain. We rigorously derive the associated shape derivative in variational form and provide explicit expressions for the gradient and second-order information. Optimization is carried out using a Sobolev gradient method within a finite element framework. To address difficulties in reconstructing obstacles with concave boundaries, particularly under measurement noise and the combined effects of advection and diffusion, we introduce a numerical scheme inspired by the Alternating Direction Method of Multipliers (ADMM). In addition to implementing this non-conventional approach, we demonstrate how the adjoint method can be efficiently applied and utilize *partial* gradients to develop a more efficient CCBM–ADMM scheme. The accuracy and robustness of the proposed computational approach are validated through various numerical experiments.

*Keywords:* Alternating direction method of multipliers, advection-diffusion model, coupled complex boundary method, inverse geometric problem, shape optimization, shape derivatives, adjoint method

## 1 Introduction

The advection–diffusion equation is a fundamental model in applied mathematics, describing the combined effects of transport and dispersion of substances within a medium [43]. It arises in key environmental applications, such as the spread of pollutants in air and water and the transport of solutes in rivers and groundwater. Accurate modeling of these processes is essential for pollution control, water resource management, and related environmental systems [57].

Because of its central role in predicting and managing transport phenomena, the advection–diffusion framework has been widely studied in both theory and applications.

In recent years, significant attention has been devoted to inverse problems for advection–diffusion systems, particularly for identifying unknown shapes or sources from indirect measurements. Many works have focused on point source identification [7, 10, 11, 31, 32, 41], while others have investigated shape reconstruction using adjoint-based methods [54], domain derivative techniques [55], and topological derivatives [29]. More recently, we have studied inverse geometric problems for simplified advection–diffusion systems using conventional numerical methods [17, 18]. Building on this foundation, the present work considers a more general setting with spatially varying coefficients, and introduces a reconstruction strategy based on a non-conventional numerical shape optimization framework combined with an augmented Lagrangian method.

The objective of this paper is to recover both the solution  $u$  and an open, connected, bounded region  $\Omega \subset \mathbb{R}^d$  in an advection–diffusion problem. The domain has an annular structure,  $\Omega = D \setminus \bar{\omega}$ , where the outer boundary  $\Sigma := \partial\Omega$  is known and accessible for measurement, while the inner boundary  $\Gamma := \partial\omega$  is unknown and must be reconstructed. Here,  $D \subset \mathbb{R}^d$  represents the flow domain and  $\omega \subset D$  is an inclusion modeling an obstacle or pollutant zone. The reconstruction is based on a single pair of Cauchy data  $(f, g)$  prescribed on  $\Sigma$ , with a homogeneous Dirichlet condition imposed on the unknown boundary  $\Gamma$ . The corresponding mathematical model is the following overdetermined boundary value problem:

$$-\operatorname{div}(\sigma \nabla u) + \mathbf{b} \cdot \nabla u = 0 \text{ in } \Omega, \quad u = 0 \text{ on } \Gamma, \quad u = f, \quad \sigma \partial_{\mathbf{n}} u = g \text{ on } \Sigma, \quad (1)$$

where, in the context of pollutant transport in water,  $\sigma := \sigma(x)$ ,  $x \in D$ , denotes the diffusion coefficient,  $u := u(x)$ ,  $x \in D$ , is the contaminant concentration,  $\mathbf{b} := \mathbf{b}(x)$ ,  $x \in D$ , is the water flow velocity, and  $\partial_{\mathbf{n}} u$  denotes the outward normal derivative of  $u$  on  $\Sigma$ .

Consequently, we consider the inverse geometry problem:

$$\text{Find } \Gamma \text{ and } u \text{ that satisfy the overdetermined system (1).} \quad (2)$$

We address this problem using shape optimization [23, 37, 53], a well-established framework for free boundary problems [28], including shape identification [13, 14, 27, 33, 34]. For overdetermined systems such as (1), one typically prescribes a boundary condition on the free boundary to ensure a well-posed state equation, while the remaining data are identified via least-squares minimization [17, 18].

Here, we propose a non-conventional shape optimization method based on the *coupled complex boundary method* (CCBM) [2, 16, 45, 51, 47]. The CCBM encodes Neumann data as the real part and Dirichlet data as the imaginary part of a Robin-type complex boundary condition. The inverse problem is then solved by minimizing the  $L^2$  norm of the imaginary part of the solution over the domain, which distinguishes the CCBM from conventional methods that impose misfit penalties directly on the boundary [3, 4, 5, 6, 17, 18].

The main novelty of this study lies in extending the CCBM framework to advection–diffusion systems with spatially varying coefficients  $\sigma$  and  $\mathbf{b}$ . This setting provides a richer and more realistic description of transport phenomena compared to constant-coefficient models. In addition, we consider complex geometries, including nonconvex shapes, beyond the smooth convex cases commonly addressed in earlier works [54, 55]. Our formulation therefore broadens the applicability of these non-conventional shape reconstruction techniques to more general scenarios relevant to practical modeling.

To improve the recovery of complex-shaped obstacles under noisy data, we embed the CCBM within an augmented Lagrangian framework based on the Alternating Direction Method

of Multipliers (ADMM) [17, 50]. This provides an alternative to conventional regularization techniques such as perimeter or surface penalization. Note that existing ADMM-based shape optimization methods use real-valued auxiliary variables. In our case, the state variable is complex-valued, so the auxiliary variable must be redefined consistently and adapted to the CCBM structure. This results in a state-of-the-art ADMM algorithm specifically designed for CCBM. In addition, we propose a partial gradient scheme that further improves reconstruction accuracy while reducing computational cost. Altogether, the resulting CCBM–ADMM framework provides a unified and efficient optimization strategy, whose effectiveness is demonstrated through numerical experiments, with particular emphasis on three-dimensional configurations.

The remainder of this paper is organized as follows. Section 2 introduces the problem setting and formulates the shape optimization framework, emphasizing the application of CCBM to system (1) and addressing the existence of a shape solution. Section 3 briefly reviews the essentials of shape calculus, derives the material derivative of the state variable, and characterizes the shape gradient of the cost functional using the adjoint method. Section 4 presents a gradient-based algorithm and numerical experiments. Two-dimensional examples first illustrate the conventional shape optimization procedure with CCBM. We then introduce an ADMM approach, motivated by the increased complexity from spatially dependent coefficients, and demonstrate its advantages through three-dimensional examples. Section 5 concludes the paper, while Appendix A provides derivations of key formulas and Appendix B presents the derivation of the shape derivative of the Lagrangian functional associated with the proposed ADMM formulation.

## 2 The problem setting

Let us first fix notations for function spaces and norms. We use the standard Lebesgue and Sobolev spaces:  $W^{m,p}(\Omega) = \{u \in L^p(\Omega) \mid D^\alpha u \in L^p(\Omega), \forall \alpha \in \mathbb{N}^d, |\alpha| \leq m\}$ . Accordingly, we write  $W^{0,p}(\Omega) = L^p(\Omega)$  and  $H^m(\Omega) = W^{m,2}(\Omega)$ , with the inner product  $\langle u, v \rangle_{m,\Omega} = \sum_{|\alpha| \leq m} \int_\Omega D^\alpha u D^\alpha v dx$  and the norm  $\|u\|_{H^m(\Omega)}^2 = \langle u, u \rangle_{m,\Omega}$ . For complex-valued functions, we use  $\mathbf{H}^m(\Omega)$ , with the inner product  $((u, v))_{m,\Omega} = \sum_{|\alpha| \leq m} \int_\Omega D^\alpha u \overline{D^\alpha v} dx$  and the norm  $\|u\|_{\mathbf{H}^m(\Omega)}^2 = ((u, u))_{m,\Omega}$ . We also introduce the subspaces  $V(\Omega) := \{\varphi \in H^1(\Omega) \mid \varphi = 0 \text{ on } \Gamma\}$  and  $\mathbf{V}(\Omega) := \{\varphi \in \mathbf{H}^1(\Omega) \mid \varphi = 0 \text{ on } \Gamma\}$ . Moreover, we define  $Q = L^2(\Omega)$  and  $\mathbf{Q} = \mathbf{L}^2(\Omega)$ . We equip the space  $\mathbf{V}(\Omega)$  with the norm  $\|\varphi\|_{\mathbf{V}(\Omega)} = \sqrt{\|\nabla \varphi\|_{\mathbf{Q}^d}}$ . Throughout the paper,  $c > 0$  denotes a generic positive constant, whose value may change from line to line.

### 2.1 Key assumptions and the inverse geometry problem

**Assumption 2.1.** *We consider Equation (1) under the following assumptions:*

- (i)  $\sigma \in W^{1,\infty}(D)^{d \times d}$  and there is  $\sigma_0 \in \mathbb{R}_+$  such that  $\sum_{i,j=1}^d \sigma_{ij} \xi_i \xi_j \geq \sigma_0 \|\xi\|_d^2$ , for any  $\xi \in \mathbb{R}^d$ ;
- (ii)  $\mathbf{b} \in W^{1,\infty}(D)^d$ ;
- (iii)  $f \in H^{3/2}(\Sigma)$  with  $f \not\equiv 0$ , and  $g \in H^{1/2}(\Sigma)$  is the corresponding compatible boundary measurement;
- (iv) there exists a constant  $c > 0$  such that  $|\mathbf{b}|_{L^\infty(D)^d} < c\sigma_0$ .

To simplify the analysis and notation, we assume that  $\sigma \in W^{1,\infty}(D)^{1 \times 1}$ , i.e.,  $\sigma$  is scalar. We denote  $b_\infty := |\mathbf{b}|_{L^\infty(D)^d}$ , and we work throughout the paper under Assumption 2.1, unless stated otherwise.

We fix some notations used throughout this paper. Let  $D \subset \mathbb{R}^d$ ,  $d \in \{2, 3\}$ , be a bounded open set and  $d_o > 0$ . We define an open set  $D_{d_o} \Subset D$  with  $C^\infty$  boundary satisfying  $\{x \in D : d(x, \partial D) > d_o/2\} \subset D_{d_o} \subset \{x \in D : d(x, \partial D) > d_o/3\}$ . The set of admissible obstacles is then

$$\mathcal{O} := \{\omega \Subset D_{d_o} \mid \omega \text{ is } C^{1,1} \text{ and } D \setminus \bar{\omega} \text{ is connected}\}. \quad (3)$$

A domain  $\Omega \subset \mathbb{R}^d$  is said to be *admissible* if  $\Omega = D \setminus \bar{\omega}$  for some  $\omega \in \mathcal{O}$ , in which case we write  $\Omega \in \mathcal{O}_{ad}$ . We assume the existence of  $\omega^* \in \mathcal{O}$  (equivalently  $\Omega^* \in \mathcal{O}_{ad}$ ) such that the overdetermined system (1) admits a solution. Hence, the inverse geometry problem (2) becomes

$$\text{Find } \omega \in \mathcal{O} \text{ and } u \text{ such that (1) holds.} \quad (4)$$

Unless stated otherwise, all annular domains  $\Omega$  are assumed admissible under Assumption 2.1.

## 2.2 The coupled complex boundary value problem

To address the inverse geometry problem (4), we adopt a non-conventional shape optimization approach based on the *coupled complex boundary method* (CCBM) [16]. Unlike traditional least-squares methods that fit boundary data directly and may suffer from numerical instabilities, CCBM relocates the data fitting to the domain interior. This naturally leads to a cost functional defined as a domain integral, which improves stability and robustness in the reconstruction process, in a manner comparable to the Kohn–Vogelius method [38].

The main idea of CCBM is to encode the measured Dirichlet and Neumann data into a complex-valued Robin boundary condition, with the real and imaginary parts representing these measurements. This formulation regularizes the inverse problem, providing stable and accurate reconstructions even in the presence of noise, while increasing the size of the resulting system. CCBM has been successfully applied to various inverse problems, including conductivity reconstruction, parameter identification in elliptic equations, free boundary problems, and tumor localization [2, 16, 30, 44, 45, 47, 51, 46, 56].

To implement CCBM, system (1) is reformulated as the following complex-valued boundary value problem:

$$-\operatorname{div}(\sigma \nabla u) + \mathbf{b} \cdot \nabla u = 0 \quad \text{in } \Omega, \quad u = 0 \quad \text{on } \Gamma, \quad \sigma \partial_{\mathbf{n}} u + iu = g + if \quad \text{on } \Sigma, \quad (5)$$

where  $u : \Omega \rightarrow \mathbb{C}$  and  $i = \sqrt{-1}$ . Hereinafter, unless otherwise specified,  $u = u(\Omega)$  will always denote the solution of (5).

Let the sesquilinear form  $a : \mathbf{V}(\Omega) \times \mathbf{V}(\Omega) \rightarrow \mathbb{C}$  and the linear form  $l : \mathbf{V}(\Omega) \rightarrow \mathbb{C}$  be

$$a(\varphi, \psi) = \int_{\Omega} \sigma \nabla \varphi \cdot \nabla \bar{\psi} + (\mathbf{b} \cdot \nabla \varphi) \bar{\psi} dx + i \int_{\Sigma} \varphi \bar{\psi} ds, \quad (6)$$

$$l(\psi) = \int_{\Sigma} (g + if) \bar{\psi} ds, \quad \forall \varphi, \psi \in \mathbf{V}(\Omega). \quad (7)$$

The weak formulation of (5) reads:

$$\text{Find } u \in \mathbf{V}(\Omega) \text{ such that } a(u, \psi) = l(\psi) \text{ for all } \psi \in \mathbf{V}(\Omega). \quad (8)$$

Existence and uniqueness of  $u$  follow from the complex Lax-Milgram lemma [21, p. 368], using the coercivity condition  $\Re(a(\varphi, \varphi)) \geq (\sigma_0 - cb_\infty) \|\varphi\|_{\mathbf{V}(\Omega)}^2$ , where  $c > 0$  depends on the Poincaré–Friedrichs constant  $c_P > 0$ . Moreover, if  $(f, g) \in H^{3/2}(\Sigma) \times H^{1/2}(\Sigma)$ , then  $u \in \mathbf{H}^2(\Omega) \cap \mathbf{V}(\Omega)$ .

Let us write  $u = u_1 + iu_2 := \Re\{u\} + i\Im\{u\}$ , where  $u_1, u_2 : \Omega \rightarrow \mathbb{R}$ . Then, we can split the complex PDE (5) into the following coupled system of real PDEs

$$\begin{cases} -\operatorname{div}(\sigma \nabla u_1) + \mathbf{b} \cdot \nabla u_1 = 0 & \text{in } \Omega, \\ u_1 = 0 & \text{on } \Gamma, \\ \sigma \partial_{\mathbf{n}} u_1 - u_2 = g & \text{on } \Sigma, \end{cases} \quad (\text{Re})$$

$$\begin{cases} -\operatorname{div}(\sigma \nabla u_2) + \mathbf{b} \cdot \nabla u_2 = 0 & \text{in } \Omega, \\ u_2 = 0 & \text{on } \Gamma, \\ \sigma \partial_{\mathbf{n}} u_2 + u_1 = f & \text{on } \Sigma. \end{cases} \quad (\text{Im})$$

Observe from (Re) and (Im) that if  $u_2 = 0$  in  $\Omega$ , then  $u_2 = \partial_{\mathbf{n}} u_2 = 0$  on  $\Sigma$ ,  $u_1 = u = 0$  on  $\Gamma$ , and  $u_1 = u = f$ ,  $\partial_{\mathbf{n}} u_1 = \partial_{\mathbf{n}} u = g$  on  $\Sigma$ . Hence,  $(\Omega, u_1)$  solves the overdetermined system (1). Conversely, any  $(\Omega, u)$  satisfying (1) ensures that  $u_1$  and  $u_2$  satisfy (Re) and (Im).

Consequently, problem (2) can be reformulated as follows:

**Problem 1.** Find  $(\Omega, u(\Omega)) \in \mathcal{O}_{ad} \times \mathbf{V}(\Omega)$  such that  $u_2 = \Im\{u\} = 0$  in  $\Omega$ .

To solve Problem 1, we introduce the cost functional  $J(\Omega)$ , defined by

$$J(\Omega) := \frac{1}{2} \int_{\Omega} |u_2|^2 dx. \quad (9)$$

For each fixed  $\Omega \in \mathcal{O}_{ad}$ , there exists a unique weak solution  $u(\Omega)$  to (5), so the mapping  $\Omega \mapsto u(\Omega) \in \mathbf{V}(\Omega)$  is well-defined. Hereinafter, (5) will be referred to as the state equation, and its solution simply as the state.

We can now state the shape identification problem:

**Problem 2.** Find  $\Omega^* \in \mathcal{O}_{ad}$  such that  $J(\Omega^*) = \min_{\Omega \in \mathcal{O}_{ad}} J(\Omega)$ .

**Proposition 1** (Problems 1 and 2 are equivalent). *If Problem 1 has a solution  $(u, \tilde{\Omega})$ , such that  $u_2 = 0$  in  $\tilde{\Omega} \in \mathcal{O}_{ad}$ , then Problem 1 is equivalent to Problem 2.*

*Proof.* Let  $(u, \tilde{\Omega})$  be the solution of Problem 1, such that  $u_2 = 0$  in  $\tilde{\Omega}$ , where  $\tilde{\Omega}$  is an admissible domain. We have  $J(\tilde{\Omega}) = \int_{\tilde{\Omega}} |u_2|^2 dx = 0 \leq J(\Omega)$ , for all  $\Omega \in \mathcal{O}_{ad}$ . Thus,  $(u, \tilde{\Omega})$  is a solution to Problem 2. Conversely, let  $(u^*, \Omega^*)$  be the solution of Problem 2. We have  $0 = J(\Omega^*) = \int_{\Omega^*} |u_2|^2 dx \leq J(\Omega)$ , for all  $\Omega \in \mathcal{O}_{ad}$ . For  $\Omega = \tilde{\Omega}$ , we obtain  $0 = J(\Omega^*) = \int_{\Omega^*} |u_2|^2 dx \leq J(\tilde{\Omega}) = 0$ . Therefore,  $\int_{\Omega^*} |u_2|^2 dx = 0$ , which implies that  $u_2 = 0$  in  $\Omega^*$ . We conclude that  $(u^*, \Omega^*)$  is a solution to Problem 1.  $\square$

### 2.3 Existence of shape solution

In light of Proposition 1, we assert that Problem 2 admits a solution:

**Proposition 2.** Problem 2 admits a solution in  $\mathcal{O}_{ad}$ .

To prove Proposition 2, we require certain properties of the admissible domains. A sufficient condition is uniform regularity (see [15] or [23, Chap. 5.6.4]), known as the  $\epsilon$ -property [6], which holds since  $\Omega \in \mathcal{O}_{ad} \subset C^{1,1}$  [37, Thm. 2.4.7, p. 56]. Equipping  $\mathcal{O}_{ad}$  with the Hausdorff distance [37, Def. 2.2.7, p. 30], existence of an optimal solution follows if: (i)  $\mathcal{O}_{ad}$  is compact; (ii)  $\Omega_n \rightarrow \Omega$  in the Hausdorff sense implies  $u(\Omega_n) \rightarrow u(\Omega)$  [37, Def. 2.2.8, p. 30]; and (iii) under (i) and (ii),  $J(\Omega_n, u(\Omega_n)) \rightarrow J(\Omega, u(\Omega))$ . The proof then proceeds based on these arguments.

On  $\Gamma$ , recall that  $u = 0$ . We define  $\tilde{u} \in \mathbf{H}_\omega^1(D) := \{\psi \in \mathbf{H}^1(D) \mid \psi|_\omega = 0\}$  as the  $\mathbf{H}^1$ -smooth extension of  $u \in \mathbf{V}(\Omega)$  by zero in  $D$  [1, 37]:

$$\tilde{u} := \mathcal{E}u : \mathbf{H}^1(\Omega) \rightarrow \mathbf{H}_\omega^1(D), \quad \mathcal{E}u(x) = \begin{cases} u(x), & x \in \Omega = D \setminus \bar{\omega}, \\ 0, & x \in \bar{\omega}. \end{cases} \quad (10)$$

The extension operator  $\mathcal{E}$  is linear and bounded. Endowing  $\mathbf{H}_\omega^1(D)$  with the norm  $\|\cdot\|_{\mathbf{H}_\omega^1(D)} := \|\nabla \cdot\|_{\mathbf{L}^2(D)}$ , it can be shown that this norm is equivalent to the usual  $\mathbf{H}^1$ -norm:  $\|\varphi\|_{\mathbf{H}_\omega^1(D)} \sim \|\varphi\|_{\mathbf{H}^1(D)}$  for all  $\varphi \in \mathbf{H}_\omega^1(D)$ .

Using the extension (10), the weak form (8) becomes

$$\tilde{a}(\tilde{u}, \psi) = \int_D \sigma \nabla \tilde{u} \cdot \nabla \bar{\psi} dx + \int_D (\mathbf{b} \cdot \nabla \tilde{u}) \bar{\psi} dx + i \int_\Sigma \tilde{u} \bar{\psi} ds = \int_\Sigma (g + if) \bar{\psi} ds, \quad (11)$$

valid for all  $\psi \in \mathbf{H}_\omega^1(D)$ , with  $\tilde{u} \in \mathbf{H}_\omega^1(D)$ . Under Assumption 2.1(iv), well-posedness follows from the complex-valued Lax-Milgram Theorem.

Lemma 2.2 below establishes that  $\tilde{u}$  is bounded in  $\mathbf{H}^1(D)$ . This is used in Proposition 3 to show that  $u(\Omega_n) \rightarrow u(\Omega)$  as  $\Omega_n \xrightarrow{H} \Omega$  in the Hausdorff sense. Proposition 4 then ensures the continuity of the cost functional, i.e.,  $\lim_{n \rightarrow \infty} J(\Omega_n, u(\Omega_n)) = J(\Omega, u(\Omega))$ . For notational convenience, we set  $u_n := u(\Omega_n)$  and let  $\tilde{u}_n \in \mathbf{H}^1(D)$  denote its zero extension to  $D$ , for all  $n \in \mathbb{N} \cup \{0\}$ .

**Lemma 2.2.** *Under Assumption 2.1(iv), for any  $(\Omega, u) \in \mathcal{O}_{ad} \times \mathbf{V}(\Omega)$ , there exists a constant  $c^* > 0$  such that  $\|\tilde{u}\|_{\mathbf{H}^1(D)} \leq c^*$ , where  $\tilde{u}$  is the zero extension of  $u$  satisfying (11).*

*Proof.* Taking  $\psi = \tilde{u} \in \mathbf{H}_\omega^1(D)$  in (11), and using the continuous dependence of the state on the data, we obtain  $\tilde{a}(\tilde{u}, \tilde{u}) \leq (\|g\|_{H^{-1/2}(\Sigma)} + \|f\|_{H^{1/2}(\Sigma)}) \|\tilde{u}\|_{\mathbf{H}^{1/2}(\Sigma)}$ . Since  $\tilde{u} \in \mathbf{H}_\omega^1(D)$  (i.e.,  $\tilde{u} = 0$  in  $\bar{\omega}$ ), the generalized Poincaré-Friedrichs inequality [12] gives  $|\tilde{a}(\tilde{u}, \tilde{u})| \geq \Re\{\tilde{a}(\tilde{u}, \tilde{u})\} \geq (\sigma_0 - c_P b_\infty) \|\tilde{u}\|_{\mathbf{H}_\omega^1(D)}^2$ , for some constant  $c_P > 0$ . Then, choosing  $c = c_P^{-1}$  in Assumption 2.1(iv), applying the Sobolev embedding  $\|\cdot\|_{\mathbf{H}^{s-1/2}(\Sigma)} \leq c_s \|\cdot\|_{\mathbf{H}^s(D)}$  for  $s > 1/2$ , and using the equivalence  $\|\tilde{u}\|_{\mathbf{H}_\omega^1(D)} \sim \|\tilde{u}\|_{\mathbf{H}^1(D)}$ , we obtain  $\|\tilde{u}\|_{\mathbf{H}^1(D)} \leq c^*$ , where

$$c^* := \frac{c_s (\|g\|_{H^{-1/2}(\Sigma)} + \|f\|_{H^{1/2}(\Sigma)})}{\sigma_0 - c_P b_\infty}.$$

This concludes the proof.  $\square$

**Proposition 3.** *Let  $\{\Omega_n\}_{n \in \mathbb{N}} \subset \mathcal{O}_{ad}$  and  $\Omega \in \mathcal{O}_{ad}$  be such that  $\Omega_n \xrightarrow{H} \Omega$ . Then there exists a subsequence  $\{\tilde{u}_{n_k}\}$  of  $\{\tilde{u}_n\}$ , where each  $\tilde{u}_n$  solves (11) in  $\mathbf{H}_{\omega_n}^1(D)$ , for all  $\psi \in \mathbf{H}_{\omega_n}^1(D)$ , and a function  $u^* \in \mathbf{H}_\omega^1(D)$  such that:*

- $\tilde{u}_{n_k} \rightharpoonup u^*$  in  $\mathbf{H}^1(D)$ ,
- $u^* \in \mathbf{H}_\omega^1(D)$  satisfies (11), for all  $\psi \in \mathbf{H}_\omega^1(D)$ ,

- $u^*|_{\Omega} \in \mathbf{V}(\Omega)$  uniquely solves (8), and
- $\tilde{u}_{n_k} \rightarrow u^*$  in  $\mathbf{H}^1(D)$ .

*Proof.* Let  $\{\Omega_n\}_{n \in \mathbb{N}} \subset \mathcal{O}_{ad}$  and  $\Omega \in \mathcal{O}_{ad}$  be such that  $\Omega_n \xrightarrow{H} \Omega$ . Lemma 2.2 implies that  $\|\tilde{u}_n\|_{\mathbf{H}^1(D)} \leq c^*$ , hence the existence of a sequence  $\{\tilde{u}_n\}_{n \in \mathbb{N}}$  uniformly bounded in  $\mathbf{H}^1(D)$ . Consequently, we can extract a subsequence denoted by  $\{\tilde{u}_k\}_{k \in \mathbb{N}} = \{\tilde{u}_{n_k}\}_{k \in \mathbb{N}} \subset \{\tilde{u}_n\}_{n \in \mathbb{N}}$  such that  $\tilde{u}_k \rightharpoonup u^*$  in  $\mathbf{H}^1(D)$ . We let  $\psi \in \mathbf{V}(\Omega)$  and, by (10), denotes its zero extension in  $D$  by  $\tilde{\psi}$ . We construct, based on (10), a sequence  $\{\psi_k\}_{k \in \mathbb{N}} \subset \mathbf{H}_{\omega_k}^1(D)$ ,  $\{\omega_k\}_{k \in \mathbb{N}} = \{\omega_{n_k}\}_{k \in \mathbb{N}} \in \mathcal{O}$ , such that  $\psi_k \xrightarrow{k \rightarrow \infty} \tilde{\psi}$  in  $\mathbf{H}_{\omega}^1(D)$ .

Because  $\Omega_n \xrightarrow{H} \Omega$ , then there exists an index  $p \in \mathbb{N}$  such that, and for all  $n \geq p$ , we have

$$\int_{\Omega_n} \sigma \nabla u_n \cdot \nabla \bar{\psi}_k \, dx + \int_{\Omega_n} (\mathbf{b} \cdot \nabla u_n) \bar{\psi}_k \, dx + i \int_{\Sigma} u_n \bar{\psi}_k \, ds = \int_{\Sigma} (g + if) \bar{\psi}_k \, ds, \quad \forall \psi_k|_{\Omega_n} \in \mathbf{H}^1(\Omega_n).$$

For each  $n \in \mathbb{N}$ , we can extend  $u_n \in \mathbf{H}^1(\Omega_n)$  to  $D$  using (10) to obtain  $\tilde{u}_n \in \mathbf{H}_{\omega_n}^1(D)$  satisfying

$$\tilde{a}(\tilde{u}_n, \psi_k) = \int_{\Sigma} (g + if) \bar{\psi}_k \, ds, \quad \forall \psi_k \in \mathbf{H}_{\omega_n}^1(D).$$

Taking another subsequence if necessary, we know that  $u_n \rightharpoonup u^*$  in  $\mathbf{H}_{\omega}^1(D)$ , and so  $\nabla u_n \rightarrow \nabla u^*$  in  $\mathbf{H}_{\omega}^1(D)$ . This allows us to get, because  $\Omega_n \xrightarrow{H} \Omega$ , the following variational equation:

$$\tilde{a}(u^*, \psi_k) = \int_{\Sigma} (g + if) \bar{\psi}_k \, ds =: \tilde{l}(\psi_k), \quad \forall \psi_k \in \mathbf{H}_{\omega}^1(D).$$

Therefore, using the compactness of the trace operator from  $\mathbf{H}^1(D)$  to  $\mathbf{L}^2(\Sigma)$ , the Sobolev embedding  $\|\cdot\|_{\mathbf{H}^{s-1/2}(\Sigma)} \leq c_s \|\cdot\|_{\mathbf{H}^s(D)}$  for  $s > 1/2$ , and Lemma 2.2, we obtain the following convergences:

$$\begin{cases} |\tilde{a}(u^*, \psi_k) - \tilde{a}(u^*, \tilde{\psi})| \leq c^* \left( \sup_D |\sigma| + b_\infty + c \right) \|\psi_k - \tilde{\psi}\|_{\mathbf{H}_{\omega}^1(D)} \xrightarrow{k \rightarrow \infty} 0, \\ |\tilde{l}(\psi_k) - \tilde{l}(\tilde{\psi})| \leq c c_s \left( \|g\|_{H^{-1/2}(\Sigma)} + \|f\|_{H^{1/2}(\Sigma)} \right) \|\psi_k - \tilde{\psi}\|_{\mathbf{H}_{\omega}^1(D)} \xrightarrow{k \rightarrow \infty} 0, \end{cases} \quad (12)$$

for some constant  $c > 0$ . This means that  $\tilde{a}(u^*, \psi_k) \xrightarrow{k \rightarrow \infty} \tilde{a}(u^*, \tilde{\psi})$  and  $\tilde{l}(\psi_k) \xrightarrow{k \rightarrow \infty} \tilde{l}(\tilde{\psi})$ . Thus,  $\tilde{a}(u^*, \tilde{\psi}) = \tilde{l}(\tilde{\psi})$ , for all  $\tilde{\psi} \in \mathbf{H}_{\omega}^1(D)$ . The convergences in (12) and the equivalence  $\|\varphi\|_{\mathbf{H}_{\omega}^1(D)} \sim \|\varphi\|_{\mathbf{H}^1(D)}$  for functions  $\varphi \in \mathbf{H}_{\omega}^1(D)$  also tell us that  $u^* \in \mathbf{H}^1(D)$  satisfies

$$\tilde{a}(u^*, \tilde{\psi}) = \tilde{l}(\tilde{\psi}), \quad \forall \tilde{\psi} \in \mathbf{H}^1(D). \quad (13)$$

Observe that, by restricting the functions in  $\Omega$ , we can verify that  $u^*|_{\Omega} \in \mathbf{V}(\Omega)$ . Indeed, let us write  $\omega^c = D \setminus \Omega$  and  $\omega_n^c = D \setminus \Omega_n$ . We observe that  $\int_{\omega_n^c} |\tilde{u}_n|^2 \, dx = 0$  and  $\int_{\omega_n^c} |\tilde{u}_n|^2 \, dx \rightarrow \int_{\omega^c} |u^*|^2 \, dx$ . Hence,

$$\left| \int_{\omega_n^c} |\tilde{u}_n|^2 \, dx - \int_{\omega^c} |u^*|^2 \, dx \right| \leq \left| \int_D (\chi_{\omega_n^c} - \chi_{\omega^c}) |u^*|^2 \, dx \right| + \left| \int_D \chi_{\omega_n^c} (|\tilde{u}_n|^2 - |u^*|^2) \, dx \right| =: \Psi_1^n + \Psi_2^n.$$

Since  $|u^*|^2 \in \mathbf{L}^1(D)$  and  $\chi_{\omega_n^c} \rightarrow \chi_{\omega^c}$  in  $L^\infty(D)$ -weak-\* (see [37, Prop. 2.2.28, p. 45] or [6, Eq. (29)]), then  $\Psi_1^n \xrightarrow{n \rightarrow \infty} 0$ . Because  $\tilde{u}_n \rightharpoonup u^*$  in  $\mathbf{H}^1(D)$  and  $\mathbf{H}^1(D) \hookrightarrow \mathbf{L}^2(D)$ , we infer

that  $\tilde{u}_n \rightarrow u^*$  in  $\mathbf{L}^2(D)$ . By Lemma 2.2, we also see that  $\Psi_2^n \leq \int_D |\tilde{u}_n|^2 - |u^*|^2 dx \xrightarrow{n \rightarrow \infty} 0$ . Therefore  $\int_{\omega^c} |u^*|^2 dx = 0$ , and we conclude that  $u^* \in \mathbf{V}(\Omega)$ . Now, going back to (13), we see that

$$a(u^*|_\Omega, \psi) = l(\psi), \quad \forall \psi = \tilde{\psi}|_\Omega \in \mathbf{V}(\Omega). \quad (14)$$

Finally, we will show the strong convergence  $\tilde{u}_n \rightarrow u^*$  in  $\mathbf{H}^1(D)$ . To do this, let us denote  $w_n = \tilde{u}_n - u^*$ . On the one hand, from (13), with  $\psi = w_n = \tilde{u}_n - u^* \in \mathbf{H}^1(D)$ , we have

$$\tilde{a}(u^*, w_n) = \tilde{l}(w_n). \quad (15)$$

On the other hand, we also have that

$$\int_{\Omega_n} \sigma \nabla u_n \cdot \nabla (\overline{w_n|_{\Omega_n}}) dx + \int_{\Omega_n} (\mathbf{b} \cdot \nabla u_n) \overline{(w_n|_{\Omega_n})} dx + i \int_{\Sigma} u_n \overline{(w_n|_{\Omega_n})} ds = \int_{\Sigma} (g + if) \overline{(w_n|_{\Omega_n})} ds.$$

Extending all functions to  $D$  via (10), we get

$$\tilde{a}(\tilde{u}_n, w_n) = \tilde{l}(w_n). \quad (16)$$

Subtracting (15) from (16), we get

$$\Psi(w_n) := \int_D \sigma \nabla w_n \cdot \nabla \overline{w_n} dx + \int_D \mathbf{b} \cdot \nabla w_n \overline{w_n} dx = -i \int_{\Sigma} w_n \overline{w_n} ds.$$

Clearly, because  $w_n = \tilde{u}_n - u^* \in \mathbf{H}^1(D)$  vanishes on a subdomain of  $D$ , we can apply Poincaré-Friedrich's inequality to obtain

$$0 \leq c(\sigma_0 - c_P b_\infty) \|\tilde{u}_n - u^*\|_{\mathbf{H}^1(D)}^2 \leq (\sigma_0 - c_P b_\infty) \|\nabla w_n\|_{\mathbf{L}^2(D)^d}^2 \leq |\Psi(w_n)| \leq \|\tilde{u}_n - u^*\|_{\mathbf{L}^2(\Sigma)}^2,$$

for some constant  $c > 0$ .

Using the compactness of the trace operator from  $\mathbf{H}^1(D)$  into  $\mathbf{L}^2(\Sigma)$ , we can extract a subsequence, still denoted by  $\{\tilde{u}_n\}_{n \in \mathbb{N}}$ , such that  $\tilde{u}_n|_\Sigma \rightharpoonup u^*|_\Sigma$  in  $\mathbf{L}^2(\Sigma)$ . Consequently, we get

$$0 \leq \|\tilde{u}_n - u^*\|_{\mathbf{H}^1(D)}^2 \leq \frac{1}{c(\sigma_0 - c_P b_\infty)} \|\tilde{u}_n - u^*\|_{\mathbf{L}^2(\Sigma)}^2 \xrightarrow{n \rightarrow \infty} 0.$$

In conclusion,  $\tilde{u}_n$  converges strongly to  $u^*$  in  $\mathbf{H}^1(D)$ . This completes the proof of the proposition.  $\square$

**Proposition 4.** *Under the assumptions of Proposition 3, we have  $\lim_{n \rightarrow +\infty} J(\Omega_n) = J(\Omega)$ .*

The proof follows similar arguments to those employed in Proposition 3 and is therefore omitted.

## 3 Shape Sensitivity Analysis

### 3.1 Shape perturbations and material derivative

To numerically solve Problem 2, we use a shape-gradient method with the finite element method (FEM), which requires the shape derivative of  $J$ . In this section, we derive this expression using *shape calculus* [23, 37, 40, 52, 53], specifically via a chain-rule approach based on the

*material* derivative of the solution to (5). For this purpose, we let  $\Theta$  be the space of admissible deformation fields  $\boldsymbol{\theta}$ :

$$\Theta := \{\boldsymbol{\theta} \in C^{1,1}(\overline{D}, \mathbb{R}^d) \mid \text{supp}(\boldsymbol{\theta}) \subseteq \overline{D}_\delta\}.$$

We let  $\theta_n = \langle \boldsymbol{\theta}, \mathbf{n} \rangle$ , where  $\mathbf{n}$  is the outward unit normal vector to  $\Omega$ . From this point forward, we consider all deformation fields to be admissible unless indicated otherwise.

For  $t \geq 0$  and  $\boldsymbol{\theta} \in \Theta$ , we consider the operator  $T_t : \overline{D} \rightarrow \overline{D}$  [23, p. 147] defined by

$$T_t = \text{id} + t\boldsymbol{\theta}, \quad T_0(\Omega) = \Omega \in \mathcal{O}_{ad}.$$

We assume that  $t_0 > 0$  is sufficiently small so that, for all  $t \in I := [0, t_0)$ ,  $T_t$  is a  $C^{1,1}$  diffeomorphism of  $D$  onto itself with strictly positive Jacobian  $I_t := \det(DT_t) > 0$ . Thus,  $T_t$  preserves the topology and regularity of  $\Omega$  under the perturbation.

Let us denote  $A_t := I_t(DT_t^{-1})(DT_t)^{-\top}$ ,  $B_t := I_t|(DT_t)^{-\top}\mathbf{n}|$ , and  $C_t := I_t(DT_t)^{-\top}$ . We assume that, for all  $t \in I$ ,  $A_t$  and  $I_t$  are uniformly bounded and that  $A_t$  is coercive [23, p. 526]. It is straightforward to verify that the mappings  $t \mapsto I_t$ ,  $A_t$ ,  $B_t$ , and  $C_t$  are continuously differentiable, with derivatives given by [53, pp. 75–76, 79–85] (here  $\dot{Z}_0 = (d/dt)Z_t|_{t=0}$ ):

$$\begin{cases} \dot{I}_0 = \text{div } \boldsymbol{\theta}, & \dot{B}_0 = \text{div}_\tau \boldsymbol{\theta} = \text{div } \boldsymbol{\theta}|_\Sigma - (D\boldsymbol{\theta}\mathbf{n}) \cdot \mathbf{n} =: B, \\ \dot{A}_0 = (\text{div } \boldsymbol{\theta})\mathbf{I} - D\boldsymbol{\theta} - (D\boldsymbol{\theta})^\top =: A, & \dot{C}_0 = (\text{div } \boldsymbol{\theta})\mathbf{I} - (D\boldsymbol{\theta})^\top =: C, \end{cases} \quad (17)$$

where  $\text{div}_\tau$  denotes the tangential divergence operator. Note that  $B$  vanishes on  $\Sigma$  for all  $\boldsymbol{\theta} \in \Theta$ .

The state  $u(\Omega) \in \mathbf{V}(\Omega)$  has a *material derivative*  $\dot{u} = \dot{u}(\Omega)[\boldsymbol{\theta}]$  at  $\Omega \in \mathcal{O}_{ad}$  in the direction of  $\boldsymbol{\theta} \in \Theta$  if the limit

$$\dot{u} = \lim_{t \searrow 0} \frac{u^t(\Omega) - u(\Omega)}{t}, \quad u^t(x) := (u(\Omega_t) \circ T_t)(x) = ((u_{1t} + iu_{2t})(\Omega_t) \circ T_t)(x), \quad x \in \Omega,$$

exists. Notice that  $u^t$  is defined on the fixed domain  $\Omega$ .

For  $\Omega \in \mathcal{O}_{ad}$ ,  $\varphi, \psi \in \mathbf{V}(\Omega)$ , we introduce the bilinear form

$$\mathcal{M}(\varphi, \psi) := - \left\{ \int_\Omega [(\sigma A \nabla \varphi + (\nabla \sigma \cdot \boldsymbol{\theta}) \nabla \varphi) \cdot \nabla \bar{\psi} + (C^\top \mathbf{b} + D\mathbf{b}\boldsymbol{\theta}) \cdot \nabla \varphi \bar{\psi}] dx \right\}.$$

If  $\Omega = \Omega^*$ , we write  $\mathcal{M}^*(\varphi, \psi)$ .

For the state equation (5), the material derivative is given in the following lemma.

**Lemma 3.1.** *The material derivative  $\dot{u} \in \mathbf{V}(\Omega)$  uniquely satisfies*

$$a(\dot{u}, \psi) = \mathcal{M}(u, \psi), \quad \forall \psi \in \mathbf{V}(\Omega). \quad (18)$$

The proof follows standard arguments and is analogous to Proposition 3.1 in [45], so it is omitted. Part of the proof requires showing that, for  $t \in I$ , the map  $(t, \varphi, \psi) \mapsto \Phi(t, \varphi, \psi)$  is differentiable with respect to  $t$ , where the sesquilinear form  $\Phi : I \times \mathbf{V}(\Omega) \times \mathbf{V}(\Omega) \rightarrow \mathbb{R}$  is

$$\Phi(t, \varphi, \psi) = \int_\Omega \sigma^t A_t \nabla \varphi \cdot \nabla \bar{\psi} dx + \int_\Omega \mathbf{b}^t \cdot C_t \nabla \varphi \bar{\psi} dx + i \int_\Sigma B_t u \bar{\psi} ds,$$

which is continuous and coercive on  $\mathbf{V}(\Omega) \times \mathbf{V}(\Omega)$ . Coercivity is ensured by choosing  $c = \eta_1 c_P^{-1} |C_t|_\infty^{-1} > 0$  in Assumption 2.1(iv). Finally, we note that since  $\boldsymbol{\theta} \in \Theta$  vanishes on  $\Sigma$ ,  $B$  does as well, and hence the integrals over  $\Sigma$  involving  $B$  vanish.

### 3.2 Shape derivatives of the shape functional

The shape functional  $J : \Omega \rightarrow \mathbb{R}$  admits a directional Eulerian derivative at  $\Omega \in \mathcal{O}_{ad}$  in the direction  $\boldsymbol{\theta} \in \Theta$  if the limit

$$\frac{d}{dt} J(\Omega_t) \Big|_{t=0} = \lim_{t \searrow 0} \frac{J(\Omega_t) - J(\Omega)}{t} =: dJ(\Omega)[\boldsymbol{\theta}]$$

exists (cf. [23, Eq. (3.6), p. 172]). If the mapping  $\boldsymbol{\theta} \mapsto dJ(\Omega)[\boldsymbol{\theta}]$  is linear and continuous for all  $\boldsymbol{\theta} \in \Theta$ , we say that  $J$  is *shape differentiable* at  $\Omega$ , and this mapping is called the *shape gradient* of  $J$ .

Similarly, the second-order Eulerian derivative of  $J$  at  $\Omega \in \mathcal{O}_{ad} \cap C^{2,1}$  along  $\boldsymbol{\theta}, \tilde{\boldsymbol{\theta}} \in \Theta \cap C^{2,1}(\overline{D}; \mathbb{R}^d)$  is defined by

$$\lim_{t \rightarrow 0} \frac{1}{t} \left( \frac{dJ(\Omega_t(\tilde{\boldsymbol{\theta}}))[\boldsymbol{\theta}] - dJ(\Omega)[\boldsymbol{\theta}]}{t} \right) =: d^2 J(\Omega)[\boldsymbol{\theta}, \tilde{\boldsymbol{\theta}}],$$

if the limit exists [22, Def. 2.3]. We say that  $J$  is twice shape differentiable if  $d^2 J(\Omega)[\boldsymbol{\theta}, \tilde{\boldsymbol{\theta}}]$  exists for all  $\boldsymbol{\theta}$  and  $\tilde{\boldsymbol{\theta}}$  and is bilinear and continuous in both arguments; this is called the *shape Hessian* of  $J$ .

It is straightforward to verify that  $J$  is shape differentiable at  $\Omega \in \mathcal{O}_{ad}$  along  $\boldsymbol{\theta} \in \Theta$ , since  $T_t$  is a  $C^{1,1}$ -diffeomorphism and the maps  $t \mapsto I_t$  and  $t \mapsto u^t$  are differentiable. The following result characterizes the shape derivative of  $J$  via the chain rule and Lemma 3.1.

**Proposition 5** (Shape gradient of  $J$ ). *The first-order shape derivative of  $J$  is given as follows:*

$$dJ(\Omega)[\boldsymbol{\theta}] = \int_{\Gamma} G \mathbf{n} \cdot \boldsymbol{\theta} \, ds = \int_{\Gamma} G(u, p) \mathbf{n} \cdot \boldsymbol{\theta} \, ds := \int_{\Gamma} [\sigma (\partial_{\mathbf{n}} u_1 \partial_{\mathbf{n}} p_2 - \partial_{\mathbf{n}} u_2 \partial_{\mathbf{n}} p_1)] \mathbf{n} \cdot \boldsymbol{\theta} \, ds, \quad (19)$$

where  $p = p_1 + ip_2 \in \mathbf{H}^2(\Omega) \cap \mathbf{V}(\Omega)$  is the adjoint variable that uniquely solves the adjoint system

$$\begin{cases} \operatorname{div}(\sigma \nabla p) + \mathbf{b} \cdot \nabla p + (\operatorname{div} \mathbf{b})p = u_2 & \text{in } \Omega, \\ p = 0 & \text{on } \Gamma, \\ \sigma \partial_{\mathbf{n}} p + p \mathbf{b} \cdot \mathbf{n} - ip = 0 & \text{on } \Sigma. \end{cases} \quad (20)$$

The weak formulation of the adjoint system (20) is given by:

$$\text{Find } p \in \mathbf{V}(\Omega) \text{ such that } - \int_{\Omega} \{\sigma \nabla p \cdot \nabla \bar{\varphi} + (\mathbf{b} \cdot \nabla \bar{\varphi})p\} \, dx + i \int_{\Sigma} p \bar{\varphi} \, ds = \int_{\Omega} u_2 \bar{\varphi} \, dx, \forall \varphi \in \mathbf{V}(\Omega). \quad (21)$$

For later use, we write  $\mathcal{M} = \mathcal{M}(u, p)$ ; see Appendix A.

*Proof of Proposition 5.* Clearly, as a consequence of the assumptions,  $J$  is shape-differentiable and we can apply Hadamard's differentiation formula (see [23, 37, 53]) to obtain

$$dJ(\Omega)[\boldsymbol{\theta}] = \frac{1}{2} \int_{\Omega} \operatorname{div} \boldsymbol{\theta} |u_2|^2 \, dx + \int_{\Omega} u_2 \dot{u}_2 \, dx.$$

For  $\boldsymbol{\theta} \in \Theta$  and sufficiently smooth  $\psi$ , the divergence theorem tells us that

$$-\int_{\Omega} \operatorname{div} \boldsymbol{\theta} \psi \, dx = \int_{\Omega} \boldsymbol{\theta} \cdot \nabla \psi \, dx - \int_{\Gamma} \psi (\boldsymbol{\theta} \cdot \mathbf{n}) \, ds, \quad (22)$$

Putting  $\psi = |\Im\{u\}|^2 = |u_2|^2 \in W^{1,1}(\Omega)$  we deduce that

$$dJ(\Omega)[\boldsymbol{\theta}] = - \int_{\Omega} u_2 \boldsymbol{\theta} \cdot \nabla u_2 dx + \int_{\Omega} u_2 \dot{u}_2 dx. \quad (23)$$

We rewrite the above expression with the goal of replacing  $\dot{u}$  with the adjoint variable  $p$ . To start, let us take  $\varphi = \dot{u} \in \mathbf{V}(\Omega)$  in (21), to get

$$- \int_{\Omega} \{ \sigma \nabla p \cdot \nabla \bar{u} + (\mathbf{b} \cdot \nabla \bar{u}) p \} dx + i \int_{\Sigma} p \bar{u} ds = \int_{\Omega} u_2 \bar{u} dx. \quad (24)$$

Next, we choose  $\psi = p \in \mathbf{V}(\Omega)$  in (18) and note that  $B = \operatorname{div}_{\tau} \boldsymbol{\theta} = 0$  on  $\Sigma$ , for any  $\boldsymbol{\theta} \in \Theta$ , to obtain  $a(\dot{u}, p) = \mathcal{M}(u, p)$ . Comparing this equation with the sesquilinear form  $a$  given in (6), with  $\varphi = \dot{u}$  and  $\psi = p$ , we arrive at the equation  $a(\dot{u}, p) = \mathcal{M}(u, p) = \mathcal{M}$ .

Now, conjugating Equation (24) gives (after computations detailed in Appendix A):

$$- \int_{\Omega} u_2 \dot{u} dx = \mathcal{M} = - \int_{\Omega} u_2 \boldsymbol{\theta} \cdot \nabla u dx + \int_{\Gamma} \sigma \partial_{\mathbf{n}} u \partial_{\mathbf{n}} \bar{p} \theta_n ds. \quad (25)$$

Finally, by comparing the imaginary parts on both sides of this equation and returning to (23), we obtain the desired shape derivative:

$$dJ(\Omega)[\boldsymbol{\theta}] = - \int_{\Omega} u_2 \boldsymbol{\theta} \cdot \nabla u_2 dx + \int_{\Omega} u_2 \dot{u}_2 dx = \int_{\Gamma} \{ \sigma (\partial_{\mathbf{n}} u_1 \partial_{\mathbf{n}} p_2 - \partial_{\mathbf{n}} u_2 \partial_{\mathbf{n}} p_1) \} \mathbf{n} \cdot \boldsymbol{\theta} ds.$$

□

**Remark 1** (Necessary condition). Assume  $\Omega^* \in \mathcal{O}_{ad}$  solves Problem 1, i.e.,  $u_2 = 0$  in  $\Omega^*$ ; then  $\Omega^*$  is stationary for Problem 2, hence  $dJ(\Omega^*)[\boldsymbol{\theta}] = 0$  for all  $\boldsymbol{\theta} \in \Theta$ .

From now on,  $\Omega^* \in \mathcal{O}_{ad}$  is called a *critical shape* of  $J$  if it satisfies Remark 1.

### 3.3 Second-order shape derivative of the cost function at the critical shape

In this section, we derive the second-order shape derivative of the cost function using the material derivatives of  $u$  and  $p$ . Direct computation via the shape derivatives of  $u$  and  $p$  requires  $u, p \in \mathbf{H}^3(\Omega) \cap \mathbf{V}(\Omega)$ , which holds if  $\Omega \in \mathcal{O}_{ad} \cap C^{2,1}$  and  $(f, g) \in H^{5/2}(\Omega) \times H^{3/2}(\Omega)$  [9]. By contrast, expressing the second-order derivative in terms of material derivatives relaxes this requirement, allowing  $\Omega \in C^{1,1}$ .

**Proposition 6** (Shape Hessian of  $J$ ). Assume that  $\Omega, \boldsymbol{\theta}, \tilde{\boldsymbol{\theta}}$ , and the Cauchy pair  $(f, g)$  possess sufficient regularity and are admissible so that  $J$  is twice shape differentiable. Then, its shape Hessian at a critical shape  $\Omega^*$  is given by

$$d^2 J(\Omega^*)[\boldsymbol{\theta}, \tilde{\boldsymbol{\theta}}] = \int_{\Gamma^*} h[\tilde{\boldsymbol{\theta}}] \mathbf{n} \cdot \boldsymbol{\theta} ds = \int_{\Gamma^*} \sigma \partial_{\mathbf{n}} w_2[\tilde{\boldsymbol{\theta}}] \partial_{\mathbf{n}} u_1 \mathbf{n} \cdot \boldsymbol{\theta} ds,$$

where  $u_2 = \Im\{u\}$ ,  $u$  solves (5) with  $\Omega = \Omega^*$ , and  $w = w_1 + iw_2 = \Re\{w\} + i\Im\{w\} \in \mathbf{H}^2(\Omega^*) \cap \mathbf{V}(\Omega^*)$ . The adjoint variable  $w$  satisfies the following problem

$$\left\{ \begin{array}{ll} \operatorname{div}(\sigma \nabla w) + \mathbf{b} \cdot \nabla w + (\operatorname{div} \mathbf{b}) w &= \dot{u}_{2,\tilde{\boldsymbol{\theta}}} \quad \text{in } \Omega^*, \\ w &= 0 \quad \text{on } \Gamma^*, \\ \sigma \partial_{\mathbf{n}} w + w \mathbf{b} \cdot \mathbf{n} - iw &= 0 \quad \text{on } \Sigma. \end{array} \right. \quad (26)$$

**Remark 2.** Notice that  $w$  is simply the derivative of  $p$  with respect to  $\tilde{\boldsymbol{\theta}} \in \Theta$  while  $\dot{u}_{2,\tilde{\boldsymbol{\theta}}}$  is the derivative of  $p$  with respect to  $\tilde{\boldsymbol{\theta}}$  (cf. [48, 45]).

*Proof.* Our assumptions ensure the existence of  $\ddot{u}_{2,\boldsymbol{\theta},\tilde{\boldsymbol{\theta}}} \in H^1(\Omega)$ . Then, differentiating  $J$  twice with respect to  $\Omega$ , first along  $\boldsymbol{\theta}$  and subsequently along  $\tilde{\boldsymbol{\theta}}$ , we obtain

$$d^2 J(\Omega)[\boldsymbol{\theta}, \tilde{\boldsymbol{\theta}}] = \frac{1}{2} \int_{\Omega} \left( \operatorname{div} \boldsymbol{\theta} \operatorname{div} \tilde{\boldsymbol{\theta}} |u_2|^2 + 2 \operatorname{div} \boldsymbol{\theta} u_2 \dot{u}_{2,\tilde{\boldsymbol{\theta}}} \right) dx + \int_{\Omega} (\dot{u}_{2,\boldsymbol{\theta}} \dot{u}_{2,\tilde{\boldsymbol{\theta}}} + u_2 \ddot{u}_{2,\boldsymbol{\theta},\tilde{\boldsymbol{\theta}}}) dx.$$

At  $\Omega = \Omega^*$ , we have  $u_2 = 0$ , so we get  $d^2 J(\Omega^*)[\boldsymbol{\theta}, \tilde{\boldsymbol{\theta}}] = \int_{\Omega^*} \dot{u}_{2,\boldsymbol{\theta}} \dot{u}_{2,\tilde{\boldsymbol{\theta}}} dx$ . Our objective is to rewrite this expression in terms of an appropriate adjoint variable, eliminating  $\dot{u}_{2,\boldsymbol{\theta}}$  and  $\dot{u}_{2,\tilde{\boldsymbol{\theta}}}$ . To this end, we multiply the first equation in (26) by  $\bar{u}_{\boldsymbol{\theta}}$ , integrate over  $\Omega^*$ , and take the complex conjugate, yielding:

$$\hat{a}(\dot{u}_{\boldsymbol{\theta}}, w) := - \int_{\Omega^*} \sigma \nabla \bar{w} \cdot \nabla \dot{u}_{\boldsymbol{\theta}} dx - \int_{\Omega^*} (\mathbf{b} \cdot \nabla \dot{u}_{\boldsymbol{\theta}}) \bar{w} dx - i \int_{\Sigma} \bar{w} \dot{u}_{\boldsymbol{\theta}} ds = \int_{\Omega^*} \dot{u}_{2,\tilde{\boldsymbol{\theta}}} \dot{u}_{\boldsymbol{\theta}} dx. \quad (27)$$

Next, in (18), we set  $\psi = w$  and replace  $\dot{u}$  with  $\dot{u}_{\boldsymbol{\theta}}$ , yielding

$$a(\dot{u}_{\boldsymbol{\theta}}, w) = \mathcal{M}^*(u_{\boldsymbol{\theta}}, w),$$

where  $a$  is the sesquilinear form defined in (6) with  $\varphi = \dot{u}_{\boldsymbol{\theta}}$ ,  $\psi = w$ , and  $\Omega = \Omega^*$ . That is,

$$a(\dot{u}_{\boldsymbol{\theta}}, w) = -\hat{a}(\dot{u}_{\boldsymbol{\theta}}, w), \quad (28)$$

with  $\hat{a}$  given in (27). Equation (28) then implies

$$-\int_{\Omega^*} \dot{u}_{2,\tilde{\boldsymbol{\theta}}} \dot{u}_{\boldsymbol{\theta}} dx = \mathcal{M}^*(u_{\boldsymbol{\theta}}, w) = -\int_{\Omega^*} \dot{u}_{2,\tilde{\boldsymbol{\theta}}} \boldsymbol{\theta} \cdot \nabla u_1 dx + \int_{\Gamma^*} \sigma \partial_{\mathbf{n}} \bar{w} \partial_{\mathbf{n}} u_1 \theta_n ds.$$

Taking the imaginary parts on both sides, we finally obtain the desired expression:

$$d^2 J(\Omega^*)[\boldsymbol{\theta}, \tilde{\boldsymbol{\theta}}] = \int_{\Omega^*} \dot{u}_{2,\tilde{\boldsymbol{\theta}}} \dot{u}_{2,\boldsymbol{\theta}} dx = \int_{\Gamma^*} \sigma \partial_{\mathbf{n}} w_2[\tilde{\boldsymbol{\theta}}] \partial_{\mathbf{n}} u_1 \theta_n ds.$$

□

The preceding calculation shows that the shape Hessian at a critical shape can be obtained without computing the state's shape derivative, though an appropriate adjoint must be introduced. Higher regularity of the domain, deformation fields, and data is required only initially; in the final expression,  $H^2$ -regularity ensures the kernel is well-defined, specifically to interpret the traces of the normal derivatives of  $u$  and the adjoint  $w$ , for which it suffices that  $u, w \in \mathbf{H}^2(\Omega^*) \cap \mathbf{V}(\Omega^*)$ . Thus, the analysis can be restricted to  $\Omega^* \in \mathcal{O}_{ad}$ , with deformation fields in  $\Theta$  and the data regularity of Assumption 2.1.

### 3.4 Compactness of the Hessian at a critical shape

Having computed the shape Hessian at the stationary domain  $\Omega^*$ , we now analyze the stability of the shape optimization problem. In particular, we show its ill-posedness by demonstrating the lack of coercivity of the bilinear form associated with the Hessian in the energy space  $H^{1/2}(\Gamma^*)$ . For further discussion on well-posedness and ill-posedness in shape optimization, see [19, 20, 26, 28].

The main result of this subsection is:

**Proposition 7** (Compactness at a critical shape). *The Riesz operator corresponding to the shape Hessian  $d^2J(\Omega^*)$  defined from  $H^{1/2}(\Gamma^*)$  to  $H^{-1/2}(\Gamma^*)$  is compact.*

*Proof.* For  $\Omega^* \in \mathcal{O}_{ad}$  and  $\boldsymbol{\theta}, \tilde{\boldsymbol{\theta}} \in \Theta \subset C^{1,1}(\overline{D}; \mathbb{R}^d)$ , we have  $\theta_n = \boldsymbol{\theta} \cdot \mathbf{n}$ ,  $\tilde{\theta}_n = \tilde{\boldsymbol{\theta}} \cdot \mathbf{n} \in H^{1/2}(\Gamma^*)$ ,  $\partial_{\mathbf{n}} u_1 \in H^{1/2}(\Gamma^*)$ , and  $\partial_{\mathbf{n}} w_2[\tilde{\boldsymbol{\theta}}] \in H^{1/2}(\Gamma^*)$ .

We introduce the following function mappings associated with  $\Gamma^*$ :

$$\begin{aligned} \mathcal{S} : H^{1/2}(\Gamma^*)^d &\longrightarrow H^{-1/2}(\Gamma^*), & \mathcal{T} : H^{1/2}(\Gamma^*)^d &\longrightarrow H^{1/2}(\Gamma^*), \\ \tilde{\boldsymbol{\theta}} &\longmapsto \sigma \partial_{\mathbf{n}} w_2[\tilde{\boldsymbol{\theta}}], & \boldsymbol{\theta} &\longmapsto \partial_{\mathbf{n}} u_1 \theta_n. \end{aligned}$$

Thus, we can write

$$d^2J(\Omega^*)[\boldsymbol{\theta}, \tilde{\boldsymbol{\theta}}] = \langle \mathcal{S}(\theta_n), \mathcal{T}(\tilde{\theta}_n) \rangle_{H^{-1/2}(\Gamma^*), H^{1/2}(\Gamma^*)} = \int_{\Gamma^*} \sigma \partial_{\mathbf{n}} w_2[\tilde{\boldsymbol{\theta}}] \partial_{\mathbf{n}} u_1 \theta_n ds.$$

On the one hand, the operator  $\mathcal{T}$  is continuous since multiplication of  $\partial_{\mathbf{n}} u_1 \in H^{1/2}(\Gamma^*)$  by the  $C^{0,1}$  function  $\theta_n$  is a continuous operation on  $H^{1/2}(\Gamma^*)$ . On the other hand, we claim that  $\mathcal{S}$  is a compact operator. To prove this claim, we decompose  $\mathcal{S}$  as  $\mathcal{S} = S_3 \circ S_2 \circ S_1 \circ S_0$ , where

$$\begin{aligned} S_0 : H^{1/2}(\Gamma^*)^d &\longrightarrow H^1(\Omega^*), & S_1 : H^1(\Omega^*) &\longrightarrow \mathbf{H}^2(\Omega^*), \\ \tilde{\boldsymbol{\theta}} &\longmapsto \dot{u}_{2,\tilde{\boldsymbol{\theta}}}, & \psi &\longmapsto w, \\ S_2 : \mathbf{H}^2(\Omega^*) &\longrightarrow H^{1/2}(\Gamma^*), & S_3 : H^{1/2}(\Gamma^*) &\longrightarrow H^{-1/2}(\Gamma^*), \\ w &\longmapsto \partial_{\mathbf{n}} w_2, & \psi &\longmapsto \sigma \psi, \end{aligned}$$

with the following properties:

- $S_0 : H^{1/2}(\Gamma^*)^d \rightarrow H^1(\Omega^*)$  is given by  $S_0(\tilde{\boldsymbol{\theta}}) = \dot{u}_{2,\tilde{\boldsymbol{\theta}}}$ , where  $\dot{u}_{2,\tilde{\boldsymbol{\theta}}} = \Im\{\dot{u}_{\tilde{\boldsymbol{\theta}}}\}$  denotes the material derivative of  $u_2 = \Im\{u\}$  in direction  $\tilde{\boldsymbol{\theta}}$ . This operator is continuous.
- $S_1 : H^1(\Omega^*) \rightarrow \mathbf{H}^2(\Omega^*)$  is defined by  $S_1(\psi) = w$ , where  $w$  solves the adjoint problem (26). Given  $\psi = \dot{u}_{2,\tilde{\boldsymbol{\theta}}} \in H^1(\Omega^*)$ ,  $\sigma \in W^{1,\infty}(D)^{d \times d}$ , and  $\mathbf{b} \in W^{1,\infty}(D)^d$ , elliptic regularity for  $\Omega^* \in C^{1,1}$  ensures  $w \in \mathbf{H}^2(\Omega^*)$  and continuity of  $S_1$ .
- $S_2 : \mathbf{H}^2(\Omega^*) \rightarrow H^{1/2}(\Gamma^*)$  is the trace operator  $S_2(w) = \partial_{\mathbf{n}} w_2$ , where  $w_2 = \Im\{w\}$ . This operator is also continuous.
- $S_3 : H^{1/2}(\Gamma^*) \rightarrow H^{-1/2}(\Gamma^*)$  is defined by  $S_3(\psi) = \sigma \psi$ , with  $\sigma \in W^{1,\infty}(D)^{d \times d}$ . Since  $\sigma|_{\Gamma^*}$  is bounded, multiplication by  $\sigma|_{\Gamma^*}$  is continuous from  $H^{1/2}(\Gamma^*)$  to  $H^{-1/2}(\Gamma^*)$ . The embedding  $H^{1/2}(\Gamma^*) \hookrightarrow H^{-1/2}(\Gamma^*)$  is compact by the Rellich–Kondrachov theorem for the  $C^{1,1}$  boundary  $\Gamma^*$  [1].

Therefore, the composition satisfies  $\mathcal{S}(\tilde{\boldsymbol{\theta}}) = S_3(S_2(S_1(S_0(\tilde{\boldsymbol{\theta}})))) = \sigma \partial_{\mathbf{n}} w_2[\tilde{\boldsymbol{\theta}}]$ . Since  $S_0$ ,  $S_1$ , and  $S_2$  are continuous and  $S_3$  involves a compact embedding, it follows that  $\mathcal{S}$  is compact, as required.  $\square$

**Remark 3.** Proposition 7 reveals the inherent instability of the optimization problem 2. Specifically, near the critical shape  $\Omega^* = D \setminus \overline{\omega^*}$  and for small perturbations  $t > 0$ , the functional  $J$  behaves as its second-order expansion. Therefore, it is not possible to guarantee an estimate like  $Ct\sqrt{J(\Omega_t)}$  with a constant  $C$  that is independent of the deformation vector field  $\boldsymbol{\theta}$ . This indicates that the shape gradient's sensitivity varies significantly with the direction of deformation, becoming ineffective for highly oscillatory perturbations where  $J$  exhibits degeneracy.

Perimeter or surface-area regularization can stabilize shape optimization under noisy data [3, 17, 48]. However, its necessity depends on boundary conditions, noise level, and shape regularity. For example, certain second-order generalized impedance conditions allow acceptable reconstructions without explicit regularization [3, 14, 13]. Alternatively, ADMM-based methods achieve stable reconstructions without classical regularization. In subsection 4.4, we introduce a tailored ADMM approach for shape identification with complex PDE constraints, enabling improved reconstructions under noisy data and for geometries with pronounced concavities.

## 4 Numerical Algorithms and Examples

We implement the proposed method using a FEM-based descent algorithm driven by the shape gradient, following [17, 18]. The first subsection summarizes the conventional numerical approach for clarity and self-containment.

### 4.1 Conventional numerical scheme for shape optimization

A natural descent direction for  $J$  is  $\boldsymbol{\theta} = -G\mathbf{n}$  with  $G \in L^2(\Gamma)$  and  $G \not\equiv 0$ . However, this may lead to unstable reconstructions and a deterioration of mesh quality due to the formation of irregular or poorly shaped elements. To address this issue, we adopt an  $H^1$ -Riesz representation of the shape gradient [25, 8]; that is, we seek  $\boldsymbol{\theta} \in H_{\Sigma,0}^1(\Omega)^d$  such that

$$c_b \int_{\Omega} \nabla \boldsymbol{\theta} : \nabla \varphi \, dx + (1 - c_b) \int_{\Gamma} \nabla_{\Gamma} \boldsymbol{\theta} : \nabla_{\Gamma} \varphi \, ds = - \int_{\Gamma} G \mathbf{n} \cdot \varphi \, ds, \quad \forall \varphi \in H_{\Sigma,0}^1(\Omega)^d, \quad (29)$$

with  $c_b \in (0, 1]$ . In this work,  $c_b$  is chosen as 0.7

The resulting Sobolev gradient [42] smoothly extends  $-G\mathbf{n}$  into  $\Omega$ , with the tangential term improving regularity. For a discussion on (discrete) shape gradient flows, we refer readers to [25].

To compute the  $k$ th domain approximation  $\Omega^k$ , we follow these steps:

**1. Initialization** Select an initial shape  $\Omega^0$ .

**2. Iteration** For  $k = 0, 1, 2, \dots$ :

2.1 Solve the state and adjoint state systems on the current domain  $\Omega^k$ .

2.2 Select a step size  $t^k > 0$  and compute the update vector  $\boldsymbol{\theta}^k$  in  $\Omega^k$ .

2.3 Update the domain via  $\Omega^{k+1} = (\text{id} + t^k \boldsymbol{\theta}^k) \Omega^k$ .

**3. Stopping Test** Repeat the iteration until a convergence criterion is satisfied.

In Step 2.2, we compute  $t^k = \mu J(\Omega^k) / |\boldsymbol{\theta}^k|_{H^1(\Omega^k)^d}^2$  following [49, p. 281], with  $\mu > 0$ , reduced if necessary to avoid mesh inversion. We set  $\mu = 0.1$  in 2D and 0.01 in 3D. The algorithm stops after a fixed number of iterations or if  $t^k < 10^{-8}$ .

We test the method in 2D and 3D. Starting with a 2D reconstruction, we examine the effects of constant and spatially varying  $\sigma$  alongside spatially varying  $\mathbf{b}$ , and introduce an ADMM modification to address observed limitations. The resulting CCBM–ADMM scheme is then applied to 3D, demonstrating robustness against non-convex obstacles and noisy data. All computations were performed on a MacBook Pro with an Apple M1 chip with 16GB RAM main memory, via FREEFEM++ [36].

## 4.2 Numerical examples in 2D

For the 2D numerical examples, the specimen is taken as a unit circle centered at the origin, with  $\sigma(x) = 1.1 + \sin(\pi x_1) \sin(\pi x_2)$  and  $\mathbf{b} = (1.1 - \sin t, 1.1 + \cos t)$  for  $t \in [0, 2\pi]$ . Synthetic data are generated from the Neumann boundary input  $g(t) = 2 + \cos t$ , with the measurement  $f = u$  taken on  $\partial\Omega$ . To avoid “inverse crimes” [39, p. 154], we use different schemes for data generation and inversion:  $p_2$  elements on a finer mesh with 300 boundary nodes for data, and  $p_1$  elements on a coarser mesh with 150 nodes ( $h = 0.05$ ) for inversion.

We consider four obstacle geometries: an ellipse, dumbbell, peanut, and L-block:

$$\begin{aligned}\Gamma_1^* &:= \{(0.1 + 0.7 \cos t, 0.2 + 0.5 \sin 2t) : t \in [0, 2\pi]\}, \\ \Gamma_2^* &:= \{(0.6 \cos t, 0.5 \sin t(1.8 + \cos 2t)) : t \in [0, 2\pi]\}, \\ \Gamma_3^* &:= \left\{ \begin{pmatrix} -0.25 + \frac{0.6 + 0.54 \cos t + 0.06 \sin 2t}{1 + 0.75 \cos t} \cos t \\ 0.05 + \frac{0.6 + 0.54 \cos t + 0.06 \sin 2t}{1 + 0.75 \cos t} \sin t \end{pmatrix}, \forall t \in [0, 2\pi] \right\}, \\ \Gamma_4^* &:= \partial\omega_L, \quad \omega_L = (-0.55, 0.55)^2 \setminus [0, 0.55]^2.\end{aligned}$$

For all cases, the algorithm starts from  $\Gamma^0 = C(\mathbf{0}, 0.6)$  and runs for 600 iterations, which provides satisfactory results without further tuning.

To test robustness against noise, we define  $u^\delta = (1 + \delta \text{ g.n.}) u^*$ , where  $u^*$  is the exact solution for input  $g$  and “g.n.” is Gaussian noise with zero mean and standard deviation  $\|u^*\|_{L^\infty(\Omega)}$ . The corresponding noisy measurement is then  $f|_\Sigma := u^\delta$ .

## 4.3 Numerical results and discussion in 2D

In this subsection, we present and discuss our numerical results for the 2D case. Figure 1 shows reconstructed shapes for several test cases, with the left and right panels corresponding to constant  $\sigma$  and spatially varying  $\sigma$ , respectively. For each case, the true inclusion, initial guess (dashed), and reconstructions from exact and noisy data are displayed. The outer black curve indicates the domain boundary, the inner black curve the true inclusion, and colored curves correspond to noise levels  $\delta = 0\%, 2\%, 5\%, 7\%$ .

Our method accurately reconstructs shapes in the noise-free case. Moderate noise reduces reconstruction quality, especially for irregular or non-convex inclusions, due to both noise and the variability of  $\sigma$  (and  $\mathbf{b}$ ); see Figure 1. Even though not shown here, similar tests indicate that spatially varying  $\mathbf{b}$  tends to yield slightly less accurate results than the constant case.

Figure 2 illustrates the L-block case, which violates the  $C^{1,1}$  regularity assumption on the obstacle. Despite this, the cost functional stabilizes after several iterations, lower final values are achieved with exact data, and gradient norms decrease with minor oscillations, confirming convergence. Thus, the reconstruction remains reasonable even for this Lipschitz-smooth obstacle.

## 4.4 Alternating Direction Method of Multipliers in shape optimization setting

In the previous discussion, we highlighted the difficulty of recovering concavities in non-convex obstacles due to noise and spatially varying diffusion and drift. To address this, we introduce an ADMM-based modification of the algorithm. This modification is applied to the 3D setting

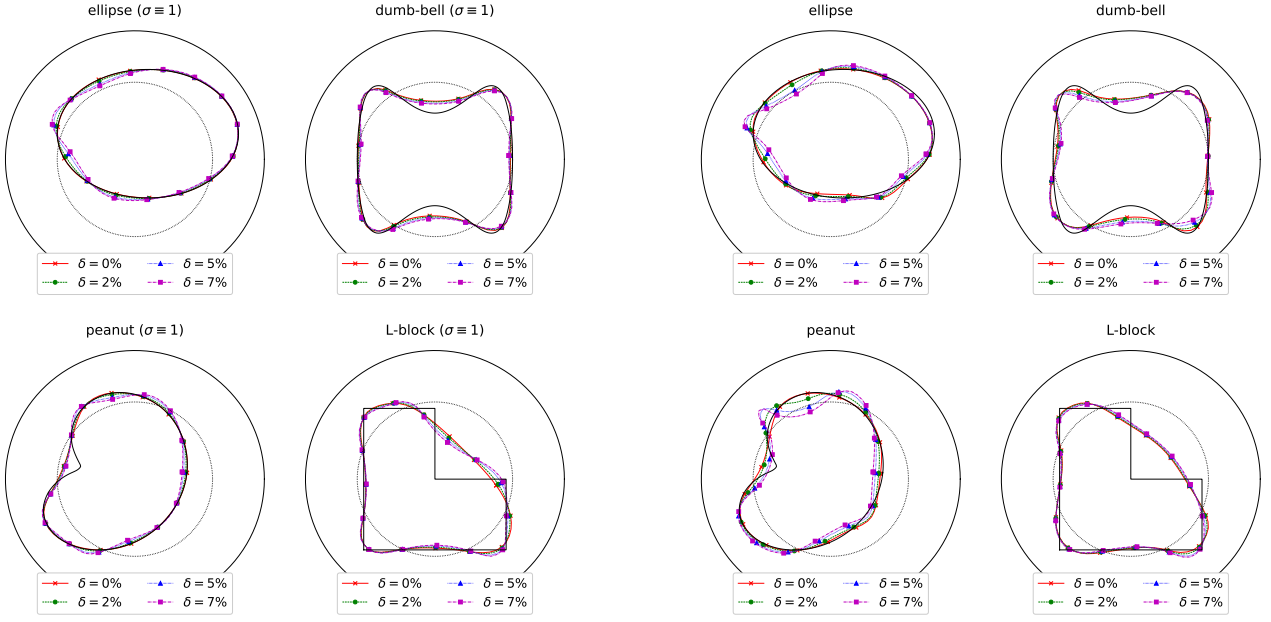


Figure 1: Results of the numerical experiments under exact and noisy measurements with noise levels  $\delta = 2\%, 5\%, 7\%$ : left, constant  $\sigma \equiv 1$ ; right, spatially varying  $\sigma(x) = 1.1 + \sin(\pi x_1) \sin(\pi x_2)$ .

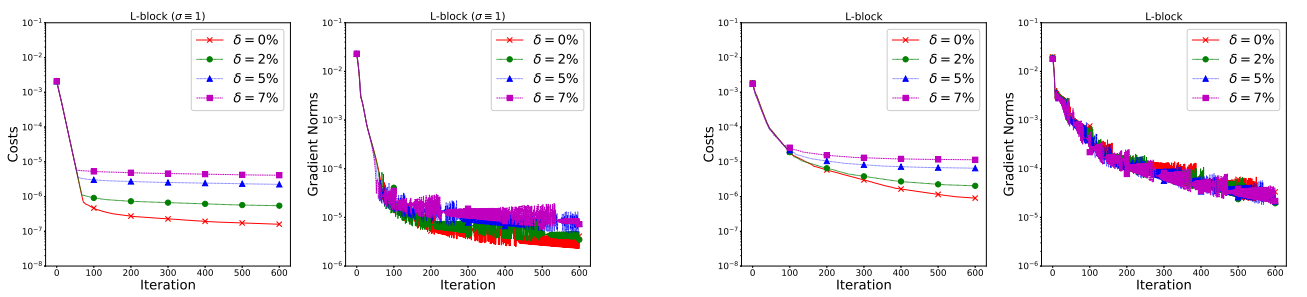


Figure 2: Cost and gradient norm histories for the L-block case: left, constant  $\sigma \equiv 1$ ; right, spatially varying  $\sigma(x) = 1.1 + \sin(\pi x_1) \sin(\pi x_2)$

in subsection 4.6 and discussed in subsection 4.7. Accordingly, we reformulate Problem 2 as follows:

**Problem 3.** Given constants  $a$  and  $b$  with  $b \geq a$ , find the shape  $\omega^*$  in the admissible set

$$\mathcal{A} = \left\{ \omega \in \mathcal{A} \mid a \leq u_1 \leq b \text{ a.e. in } \Omega \right\}$$

such that

$$\omega^* = \arg \min_{\omega \in \mathcal{A}} J(\Omega) := \arg \min_{\omega \in \mathcal{A}} \frac{1}{2} \int_{\Omega} |u_2|^2 dx. \quad (30)$$

Note that identifying  $\omega$  is equivalent to identifying  $\Omega$ , since  $\Omega = D \setminus \overline{\omega}$ , so defining one automatically determines the other.

To directly incorporate the inequality constraint in the cost function, we introduce the auxiliary variable  $v$  which satisfies  $v = u_1$  a.e. in  $\Omega$  and consider the set  $\mathcal{G}$  defined as follows:

$$\mathcal{G} = \left\{ (\omega, v) \in \mathcal{A} \times L^2(\Omega) \mid u_1 = v \text{ a.e. in } \Omega \right\}.$$

Then, we can rewrite (30) as

$$(\omega^*, v^*) = \arg \min_{(\omega, v) \in \mathcal{G}} \{J(\Omega) + U_{\mathcal{K}}(v)\}, \quad (31)$$

where the set  $\mathcal{K}$  is the closed, convex, non-empty set of  $L^2(\Omega)$  defined by

$$\mathcal{K} = \left\{ v \in L^2(\Omega) \mid a \leq v \leq b \text{ a.e. in } \Omega \right\},$$

and  $U_{\mathcal{K}}$  is the indicator functional of the set  $\mathcal{K}$ ; that is,  $U_{\mathcal{K}}(v) = 0$  if  $v \in \mathcal{K}$ , and  $U_{\mathcal{K}}(v) = \infty$  if  $v \in L^2(\Omega) \setminus \mathcal{K}$ .

To apply ADMM to the control model (31), we first define the augmented Lagrangian functional. This is possible since the minimum of problem (31) corresponds to the saddle point of the following augmented Lagrangian functional

$$L_{\beta}(\omega, v; \lambda) = J(\Omega) + U_{\mathcal{K}}(v) + \frac{\beta}{2} \int_{\Omega} |u_1 - v|^2 dx + \int_{\Omega} \lambda(u_1 - v) dx, \quad (32)$$

where  $\lambda$  is the Lagrange multiplier and  $\beta > 0$  is a penalty parameter. As in [17, 50], we fix the penalty parameter  $\beta$ . Although it is possible to optimize  $\beta$  using a bilevel approach [24], we keep it fixed to simplify the method. This choice yields consistently good results, as shown in subsection 4.7.

To find a saddle point of  $L_{\beta}$ , we employ an iterative approximation procedure based on ADMM. Starting from initial values  $\omega^0 \in \mathcal{A}$  and  $v^0, \lambda^0 \in L^2(\Omega)$ , the algorithm generates a sequence of iterates  $(\omega^k, v^k, \lambda^k)$  for  $k = 1, 2, \dots$  by solving the following minimization problems sequentially and alternately:

$$\omega^{k+1} = \arg \min_{\omega \in \mathcal{A}} L_{\beta}(\omega, v^k; \lambda^k); \quad (\text{SP1})$$

$$v^{k+1} = \arg \min_{v \in L^2(\Omega)} L_{\beta}(\omega^{k+1}, v; \lambda^k); \quad (\text{SP2})$$

$$\lambda^{k+1} = \lambda^k + \beta(u_1^{k+1} - v^{k+1}), \quad (\text{SP3})$$

where  $u_1^{k+1} := u_1(\Omega^{k+1})$ .

A concise description of the ADMM scheme is provided in Algorithm 1.

The resolution of (SP1) and (SP2) is outlined in the subsequent two subsections.

---

**Algorithm 1** ADMM algorithm for the solution of problem (30).

---

1. *Input* Fix  $\beta$ ,  $a$ , and  $b$ , and define the Cauchy pair  $(f, g)$ .
  2. *Initialization* Choose an initial shape  $\omega^0$  and set the initial values  $v^0$  and  $\lambda^0$ .
  3. *Iteration* For  $k = 1, 2, \dots$ , compute  $(\omega^k, v^k, \lambda^k)$  using equations (SP1)–(SP3) through sequential computations:
- $$\{v^k, \lambda^k\} \xrightarrow{\text{(SP1)}} \omega^{k+1} \xrightarrow{\text{(SP2)}} v^{k+1} \xrightarrow{\text{(SP3)}} \lambda^{k+1}.$$
4. *Stop Test* Repeat *Iteration* until convergence.
- 

#### 4.4.1 Solution of $\omega$ -subproblem (SP1)

We first consider the  $\omega$ -subproblem (SP1), which minimizes  $L_\beta$  with respect to  $\omega$ :

$$\omega^{k+1} = \arg \min_{\omega \in \mathcal{A}} \left\{ J(\Omega) + U_K(v^k) + \frac{\beta}{2} \int_{\Omega} |u_1 - v^k|^2 dx + \int_{\Omega} \lambda^k (u_1 - v^k) dx \right\}.$$

Consider the following shape functional:

$$Y^k(\Omega) := L_\beta(\omega, v^k; \lambda^k) = \frac{1}{2} \int_{\Omega} |u_2|^2 dx + \frac{\beta}{2} \int_{\Omega} |u_1 - v^k|^2 dx + \int_{\Omega} \lambda^k (u_1 - v^k) dx.$$

To solve the  $\omega$ -subproblem (SP1), it is necessary to compute the shape derivative of the functional  $Y^k(\Omega)$ . It is given by the following proposition whose proof is given in Appendix B.

**Proposition 8** (Shape gradient of  $Y^k(\Omega)$ ). *Let  $\Omega \in \mathcal{O}_{ad}$  and  $\boldsymbol{\theta} \in \Theta$ . Then,  $Y^k(\Omega)$  is shape differentiable, and its shape derivative at  $\Omega$  in the direction  $\boldsymbol{\theta}$  is*

$$dY^k(\Omega)[\boldsymbol{\theta}] = \int_{\Gamma} \left( \sigma(\partial_{\mathbf{n}} q_1 \partial_{\mathbf{n}} u_2 - \partial_{\mathbf{n}} q_2 \partial_{\mathbf{n}} u_1) + \frac{\beta}{2} (v^k)^2 - \lambda^k v^k \right) \theta_n ds, \quad (33)$$

where  $u = u_1 + iu_2$  satisfies (5) and the adjoint variable  $q = q_1 + iq_2 \in \mathbf{H}^2(\Omega) \cap \mathbf{V}(\Omega)$  uniquely solves the adjoint system

$$\begin{cases} \operatorname{div}(\sigma \nabla q) + \mathbf{b} \cdot \nabla q + (\operatorname{div} \mathbf{b}) q &= i(\beta(u_1 - v^k) + \lambda^k) - u_2 & \text{in } \Omega, \\ q &= 0 & \text{on } \Gamma, \\ \sigma \partial_{\mathbf{n}} q + q \mathbf{b} \cdot \mathbf{n} - iq &= 0 & \text{on } \Sigma. \end{cases} \quad (34)$$

**Remark 4.** By considering an adjoint that satisfies

$$\begin{cases} \operatorname{div}(\sigma \nabla q) + \mathbf{b} \cdot \nabla q + (\operatorname{div} \mathbf{b}) q &= (\beta(u_1 - v^k) + \lambda^k) + iu_2 & \text{in } \Omega, \\ q &= 0 & \text{on } \Gamma, \\ \sigma \partial_{\mathbf{n}} q + q \mathbf{b} \cdot \mathbf{n} - iq &= 0 & \text{on } \Sigma, \end{cases} \quad (35)$$

we obtain the following equivalent expression for the shape derivative  $dY^k(\Omega)[\boldsymbol{\theta}]$ :

$$dY^k(\Omega)[\boldsymbol{\theta}] = \int_{\Gamma} \left( -\sigma(\partial_{\mathbf{n}} q_1 \partial_{\mathbf{n}} u_1 + \partial_{\mathbf{n}} q_2 \partial_{\mathbf{n}} u_2) + \frac{\beta}{2} (v^k)^2 - \lambda^k v^k \right) \theta_n ds. \quad (36)$$

The preceding formulation of the shape gradients and their adjoint systems yields an expression that avoids material derivatives and provides a natural choice. Here, we propose an alternative formulation using a different set of adjoint variables: one for the derivative of  $u_2$  and one for  $u_1$ . The resulting shape gradient of  $Y^k$  is given in the following proposition:

**Proposition 9** (Another shape gradient structure of  $Y^k(\Omega)$ ). *Let  $\Omega \in \mathcal{O}_{ad}$  and  $\boldsymbol{\theta} \in \Theta$ . Then,  $Y^k(\Omega)$  is shape differentiable, and its shape derivative at  $\Omega$  in the direction  $\boldsymbol{\theta}$  is*

$$dY^k(\Omega)[\boldsymbol{\theta}] = \int_{\Gamma} G(u, p) \theta_n ds - \int_{\Gamma} \sigma(\partial_{\mathbf{n}} \Lambda_1 \partial_{\mathbf{n}} u_1 + \partial_{\mathbf{n}} \Lambda_2 \partial_{\mathbf{n}} u_2) \theta_n ds + \int_{\Gamma} \left( \frac{\beta}{2} (v^k)^2 - \lambda^k v^k \right) \theta_n ds, \quad (37)$$

where  $G(u, p)$  is given in (19) while the adjoint variable  $\Lambda = \Lambda_1 + i\Lambda_2 \in \mathbf{H}^2(\Omega) \cap \mathbf{V}(\Omega)$  uniquely solves the adjoint system

$$\begin{cases} \operatorname{div}(\sigma \nabla \Lambda) + \mathbf{b} \cdot \nabla \Lambda + (\operatorname{div} \mathbf{b}) \Lambda &= \beta(u_1 - v^k) + \lambda^k \quad \text{in } \Omega, \\ \Lambda &= 0 \quad \text{on } \Gamma, \\ \sigma \partial_{\mathbf{n}} \Lambda + \Lambda \mathbf{b} \cdot \mathbf{n} - i\Lambda &= 0 \quad \text{on } \Sigma. \end{cases} \quad (38)$$

The proof of this proposition is similar to that of Proposition 8 in Appendix B and is therefore omitted.

From (37), we observe that the first integral is independent of the adjoint  $\Lambda$ , while the second is independent of  $p$ . This motivates the use of “partial” shape gradients, as in [35], which addresses the exterior Bernoulli free boundary problem. Accordingly, we define four shape gradients (Table 1) for computing the deformation in our numerical scheme (Algorithm 3). The merit and benefit of these choices are demonstrated numerically in subsection 4.5, showing the advantage of selectively applying the adjoint method and using only part of the exact gradient.

#### 4.4.2 Extension and regularization of the deformation field

The shape gradient of  $Y$ , as for  $J$ , is supported only on the boundary  $\Gamma$  and may be insufficiently smooth for finite element implementation. To regularize the descent vector over  $\Omega$ , we employ the same extension–regularization technique introduced in Section 4.1 and apply the Sobolev gradient-based descent (SGBD) algorithm (Algorithm 2) to solve (SP1).

---

#### Algorithm 2 SGBD algorithm for the $\omega$ -subproblem (SP1)

---

1. *Input:* Fix  $c_b, \mu, \beta, a, b$ , and  $\varepsilon$ . Set  $\lambda^k$ , and initialize  $\Omega_0^k = \Omega^k$ ,  $u_0^k = u^k$ ,  $v_0^k = v^k$ .
  2. *Iteration:* For  $m = 0, 1, 2, \dots$ :
    - 2.1 Solve (8) and the adjoint problem (34) on the current domain  $\Omega_m^k$ .
    - 2.2 Compute  $\boldsymbol{\theta}_m^k = \boldsymbol{\theta}$ , where  $\boldsymbol{\theta} \in H_{\Sigma,0}^1(\Omega_m^k)^d$  solves (29) with  $G$  replaced by the chosen shape gradient ( $G_q^k$ ,  $G_{\sharp}^k$ ,  $G_p^k$ , or  $G_{\Lambda}^k$ ).
    - 2.3 Set  $t^k = \mu J^k(\Omega_m^k)/\|\boldsymbol{\theta}_m^k\|_{H^1(\Omega_m^k)^d}$  and update  $\Omega_{m+1}^k = \{x + t^k \boldsymbol{\theta}_m^k(x) \mid x \in \Omega_m^k\}$ .
  3. *Stopping criterion:* Repeat the iteration while  $\|dY^k(\Omega_m^k)[\boldsymbol{\theta}_m^k]\| \geq \varepsilon$ .
  4. *Output:*  $\Omega^{k+1} = \Omega_{m+1}^k$ .
- 

In Step 2.3 of Algorithm 2, the step size  $t^k$  is computed using the same strategy in Section 4.1.

#### 4.4.3 Solution of the $v$ -subproblem (SP2)

We now consider the  $v$ -subproblem (SP2), solved by minimizing  $L_\beta$  with respect to  $v$ :

$$v^{k+1} = \arg \min_{v \in L^2(\Omega)} \left\{ J(\Omega^{k+1}) + U_K(v) + \frac{\beta}{2} \int_{\Omega} |u_1^{k+1} - v|^2 dx + \int_{\Omega} \lambda^k (u_1^{k+1} - v) dx \right\}.$$

Applying the projection method, we obtain  $v^{k+1} = P_K(u_1^{k+1} + \lambda^k / \beta)$ , where  $P_K(\varphi) = \max(a, \min(b, \varphi))$  for all  $\varphi \in L^2(\Omega)$  denotes the projection onto the admissible set  $K$ .

#### 4.4.4 CCBM–ADMM–SGBD algorithm

Finally, building upon the preceding discussion, we propose a modification of Algorithm 1 for the numerical solution of Problem 3, which accounts for an inequality constraint imposed on the real component of the state. More specifically, Algorithm 1 is refined into a nested, iterative CCBM–ADMM–SGBD scheme tailored to the optimal control problem (31), as described in Algorithm 3:

---

#### Algorithm 3 CCBM–ADMM–SGBD

---

1. *Initialization:* Specify  $(f, g)$ , fix  $N \in \mathbb{N}$ ,  $\beta$ ,  $a$ ,  $b$ ,  $\mu$ ,  $c_b$ , and  $\varepsilon$ , and choose  $\omega^0$ ,  $v^0$ , and  $\lambda^0$ .
  2. *Iteration:* For  $k = 0, \dots, N$ :
    - 2.1 Compute the state solution  $u^k$  of (8) on the current domain and set  $u_1^k = \Re\{u^k\}$ , the solution of (Re) associated with  $\omega^k$ .
    - 2.2 Solve the adjoint state equation(s) corresponding to the chosen shape gradient.
    - 2.3 Update  $\omega^{k+1}$  using the gradient-descent method in Algorithm 2.
    - 2.4 Update  $v^{k+1}$  as  $v^{k+1} = \max(a, \min(u_1^{k+1} + \lambda^k / \beta, b))$ .
    - 2.5 Update  $\lambda^{k+1} = \lambda^k + \beta(u_1^{k+1} - v^{k+1})$ .
  3. *Stopping criterion:* Repeat the iteration until convergence.
- 

**Remark 5.** *The above approach naturally extends to handle noisy data. In the experiments that follow, we employ the CCBM–ADMM–SGBD scheme together with the extension-regularization method from subsection 4.1, which proves sufficient to achieve accurate reconstructions under moderate noise. Although regularization terms—such as perimeter/surface area or volume—can be incorporated into the Lagrangian with their corresponding shape derivatives in (43), they do not appear necessary in our case.*

### 4.5 Effect of adjoint formulation and partial gradient selection

Our ultimate goal is to test the proposed CCBM–ADMM–SGBD (or simply CCBM–ADMM) scheme against the conventional shape optimization approach, which applies only CCBM, using three exact obstacle geometries. Figure 3 shows the exact geometries and the initial guess, along with their corresponding mesh profiles. As before, we avoid inverse crimes by using a finer mesh and higher-order finite element space for the forward problem, while using a coarser mesh and lower-order elements for the inverse reconstruction.

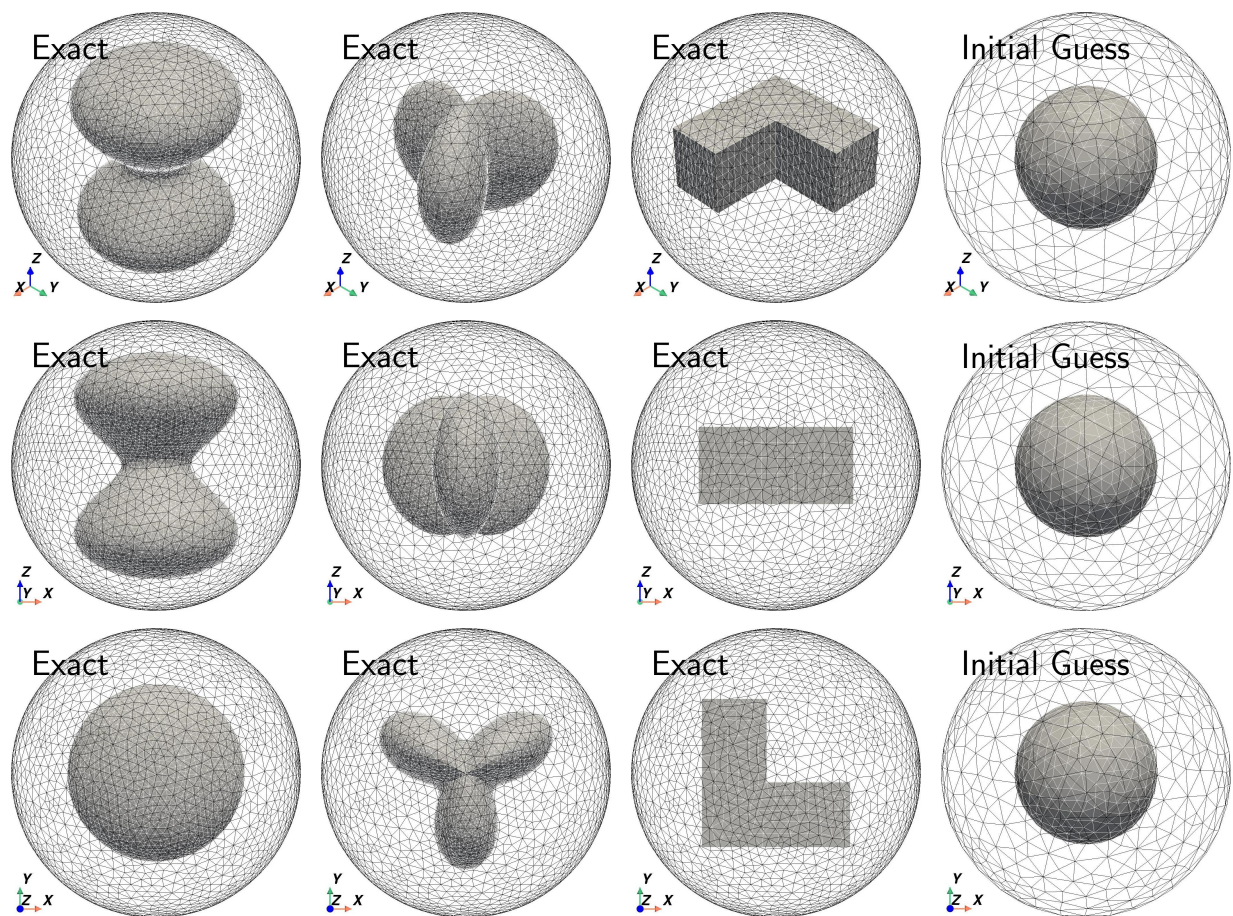


Figure 3: Geometry and mesh of the exact cavities (first three columns from the left), along with an example of an initial guess with radius  $r = 0.5$ .

Before presenting the advantages of the proposed CCBM–ADMM scheme over the conventional CCBM, we first examine the effect of the chosen shape gradient within the scheme. The motivation for this analysis stems from the particular application of the adjoint method and the use of partial, rather than exact, shape gradients.

We consider the unit ball  $D = B_1(0) \subset \mathbb{R}^3$  and write  $x = (x_1, x_2, x_3)$ . The coefficients are defined as  $\sigma(x) = 1.1 + \prod_{i=1}^3 \sin(\pi x_i)$  and  $\mathbf{b}(x) = (1, 1, 1) + 0.5x$ , with boundary data  $g(x) = e^{|x|^2}$  prescribed on  $\partial D$ . For the preliminary tests, we use an L-block-shaped obstacle and set the parameters as follows:  $N = 2400$ ,  $\lambda^0 = 0.001$ ,  $a = 0.5 \min u(\Omega \setminus \bar{\omega}^*)$ ,  $b = 1.5 \max u(\Omega \setminus \bar{\omega}^*)$ ,  $v^0 = 1$ ,  $\varepsilon = 10^{-6}$ , and  $\omega^0 = B_r(0)$  with  $r \in \{0.55, 0.575, 0.6\}$ . For each method, the selected radii, chosen from the tested range, yield the most accurate reconstructions.

We use exact measurements to clearly observe the impact of the method employed in the CCBM–ADMM scheme, whose other specifics are summarized in Table 1.

	Kernel	$r$	$\beta$
Method 1	$G_q^k := \sigma(\partial_{\mathbf{n}} q_1 \partial_{\mathbf{n}} u_2 - \partial_{\mathbf{n}} q_2 \partial_{\mathbf{n}} u_1) + \frac{\beta}{2}(v^k)^2 - \lambda^k v^k$	0.600	0.010
Method 2	$G_{\sharp}^k := G(u, p) - \sigma(\partial_{\mathbf{n}} \Lambda_1 \partial_{\mathbf{n}} u_1 + \partial_{\mathbf{n}} \Lambda_2 \partial_{\mathbf{n}} u_2) + \frac{\beta}{2}(v^k)^2 - \lambda^k v^k$	0.575	0.010
Method 3	$G_p^k := G(u, p) + \frac{\beta}{2}(v^k)^2 - \lambda^k v^k$	0.550	0.005
Method 4	$G_{\Lambda}^k := -\sigma(\partial_{\mathbf{n}} \Lambda_1 \partial_{\mathbf{n}} u_1 + \partial_{\mathbf{n}} \Lambda_2 \partial_{\mathbf{n}} u_2) + \frac{\beta}{2}(v^k)^2 - \lambda^k v^k$	0.550	0.001

Table 1: Radii and choices of  $\beta$  for each of the methods used.

The computational results for the methods listed in Table 1 are shown in Figures 4 and 5. Method 3, which employs the kernel  $G_p^k$ , delivers the most accurate obstacle reconstruction and the lowest cost functional value. While Methods 2 and 3 both capture concave regions effectively, Method 3 outperforms all others overall. In contrast, Method 1 is less sensitive to geometric features, leading to less precise reconstructions.

Method 3 also combines superior accuracy with favorable computational efficiency. For 2400 optimization iterations on a mesh with 1377 vertices, 4524 triangular elements, and 2358 boundary elements (degrees of freedom equal to the number of vertices), the CPU times for Methods 1–4 are 4267s, 4446s, 3041s, and 4187s, respectively. Thus, Method 3 is faster than Methods 1 and 4, while Method 2 is the most time-consuming.

Based on these results, we select Method 3 for further numerical experiments to benchmark the CCBM–ADMM scheme against the conventional approach using kernel  $G$  in the next subsection.

## 4.6 Numerical examples in 3D

We now consider three-dimensional examples with slightly modified space-dependent coefficients to illustrate the advantages of the ADMM framework and the influence of boundary data on the reconstruction.

The specimen is again the unit ball  $D = B_1(0) \subset \mathbb{R}^3$ ; however, we now prescribe  $\sigma(x) = 1.1 + \sin(\pi x) \sin(\pi y)$  and define

$$\mathbf{b}(x) = \left( 1.0 + 0.5 \sin \left( \arctan \left( \frac{x_2}{x_1} \right) \right), 1.0 + 0.5 \cos \left( \arctan \left( \frac{x_2}{x_1} \right) \right), 1.5 \right)^T,$$

where  $x = (x_1, x_2, x_3) \in D \subset \mathbb{R}^3$ . The boundary data are synthetically generated as  $g(x) = \exp(x_1^2 + x_2^2)$  for  $x \in \partial D$ .

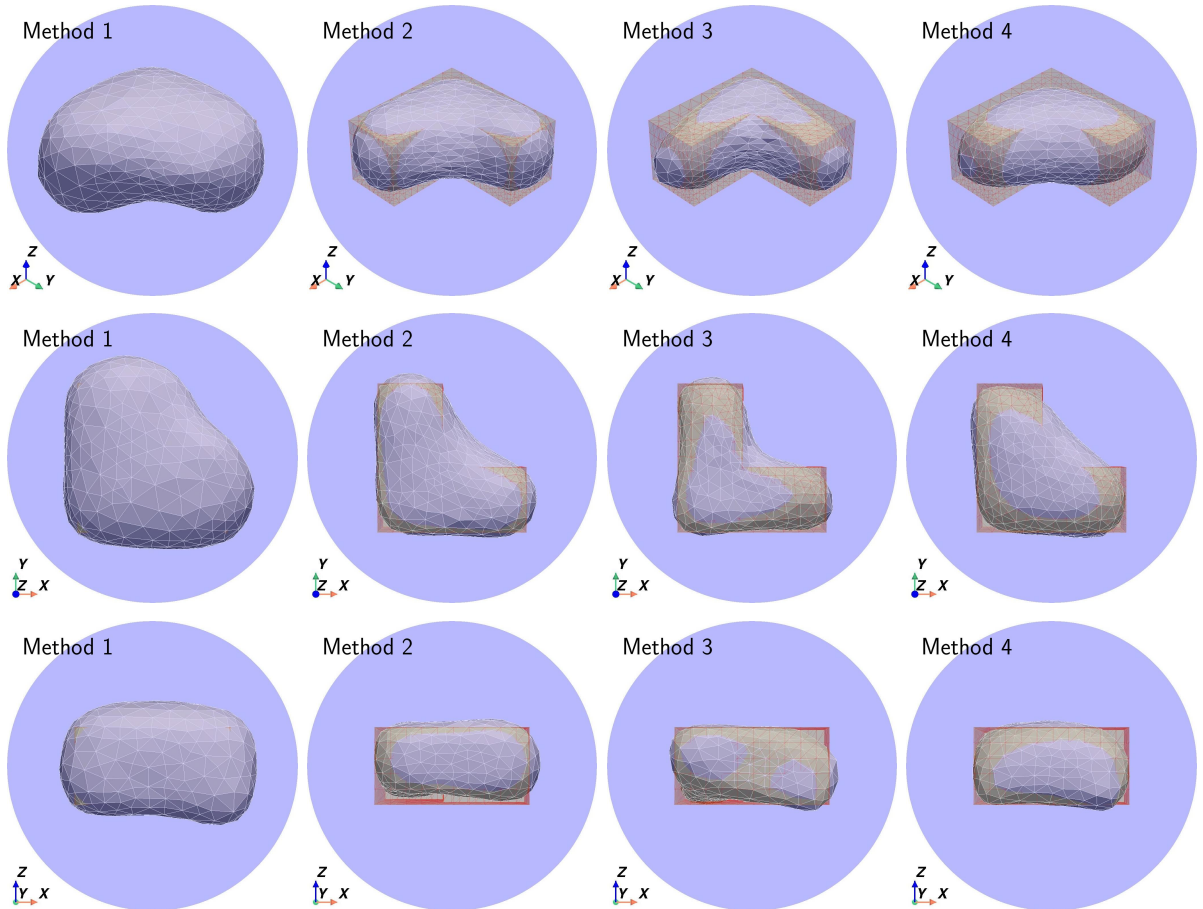


Figure 4: Effect of the adjoint formulation and partial gradient selection on the reconstructed shape

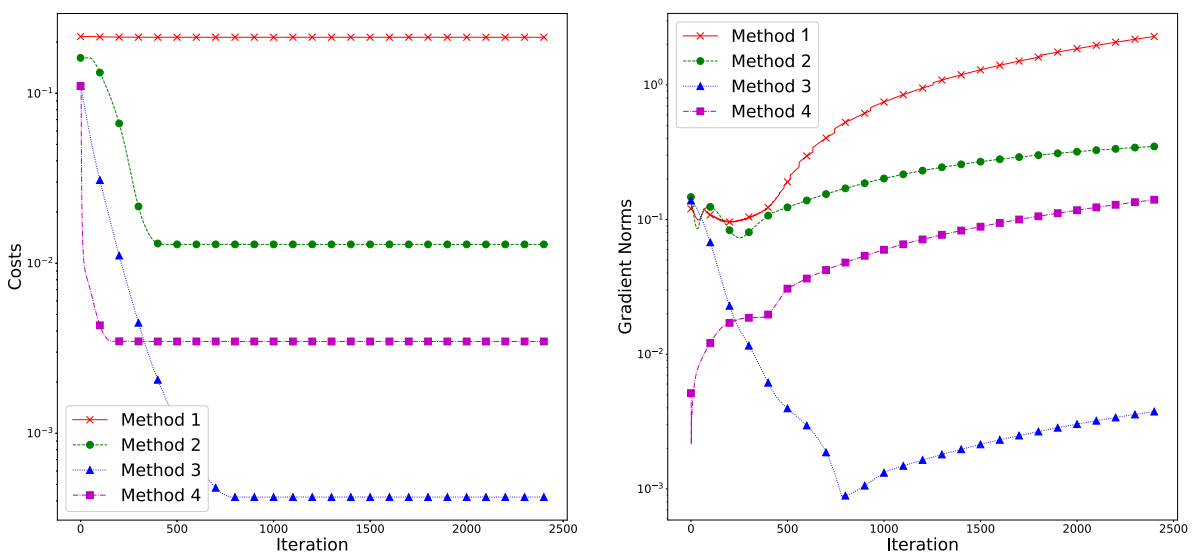


Figure 5: Cost and gradient norm histories for the reconstructed shapes in Figure 4

We compare the proposed CCBM–ADMM scheme with the conventional CCBM-based shape optimization using the three exact obstacle geometries in Figure 3. As before, inverse crimes are avoided by solving the forward problem on a finer mesh with higher-order finite elements, while using a coarser mesh and lower-order elements for reconstruction. All other computational parameters are the same as in the previous section, except  $N = 1200$  and  $\omega^0 = B_r(0)$  with  $r \in \{0.5, 0.575\}$ , chosen through preliminary testing to yield the most accurate reconstructions.

## 4.7 Numerical results and discussion in 3D

We present the results of our three-dimensional numerical experiments to demonstrate the effectiveness of the proposed CCBM–ADMM scheme.

Figures 6–8 show reconstructed shapes obtained using both the conventional CCBM and the proposed CCBM–ADMM scheme. These results highlight the difficulties of accurately recovering the underlying geometry with the naive CCBM scheme, even under exact data, and increasingly so under moderate noise. In contrast, the CCBM–ADMM scheme achieves accurate reconstructions even with moderate noise, particularly in capturing non-convex features and the depth of concavities. Notably, at high noise levels, the proposed scheme correctly identifies regions with pronounced concavities that the conventional method fails to recover (see Figures 6 and 7). The advantage of CCBM–ADMM is also evident for a Lipschitz-smooth obstacle (Figure 8), where it yields a reasonable reconstruction despite violating the smoothness assumptions of our main results.

Figure 9 illustrates the evolution of the cost functional and gradient norm for the L-block case. As expected, the cost functional converges even under moderate noise, with lower final values at reduced noise levels. The gradient norm initially decreases but later exhibits an oscillatory increase, likely due to the last two integrals in the shape gradient of  $Y^k$  (see (33)). Although not shown, the gradient norms eventually converge after further iterations.

Overall, these results underscore the robustness and effectiveness of incorporating ADMM into shape optimization, supporting previous findings [17, 50] on the potential of ADMM-based methods for challenging geometric inverse problems.

## 5 Conclusion

We have introduced a novel shape optimization method for inverse advection–diffusion problems. It embeds the coupled complex boundary method (CCBM) within an ADMM-inspired augmented Lagrangian framework. The scheme uses a Sobolev gradient method that naturally achieves mesh smoothing. As a result, it eliminates the need for explicit perimeter or surface-area regularization, which is typically required to stabilize reconstructions from noisy measurements.

Numerical experiments in two and three dimensions demonstrate accurate recovery of complex inclusion shapes, with marked improvement for concave or complex features where conventional methods struggle. By employing a carefully designed adjoint formulation alongside partial gradients, the CCBM–ADMM strategy further enhances reconstruction and consistently attains lower cost values, even when the smoothness assumptions required in the analysis are not fully satisfied.

Overall, these results highlight the effectiveness of the CCBM–ADMM framework, supporting recent evidence [17, 50] that ADMM-based methods effectively handle noisy and geometrically complex inverse shape problems.

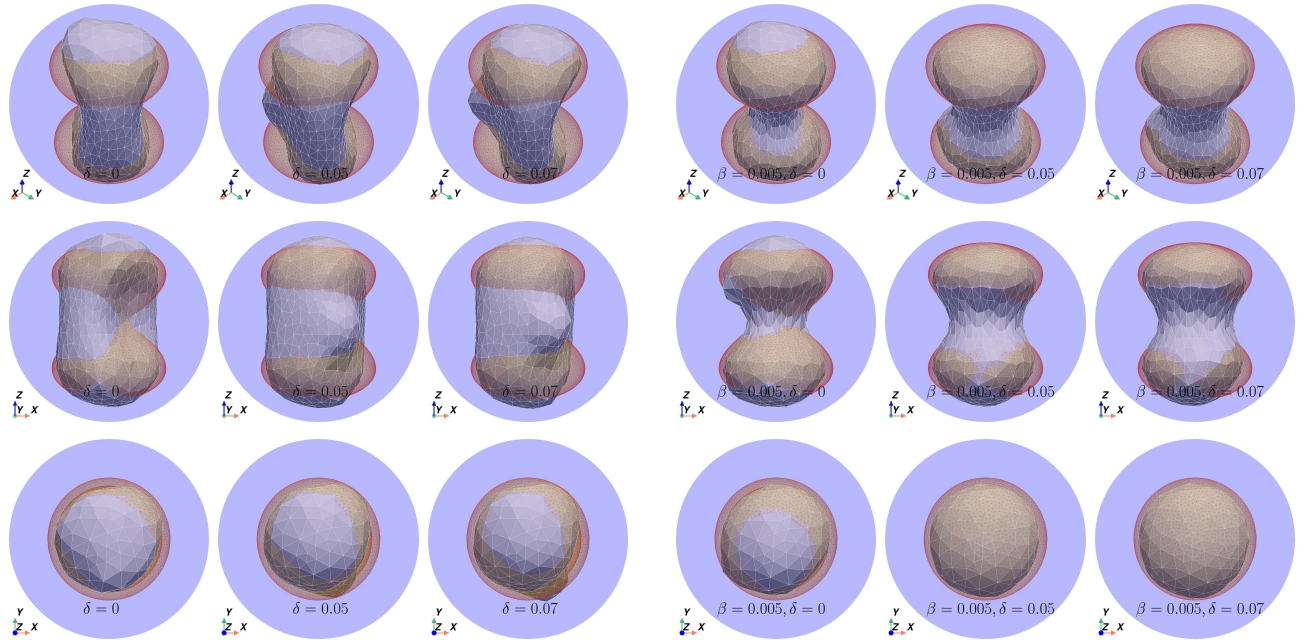


Figure 6: Reconstructed shapes using CCBM (left) and Algorithm 3 (right) under noise levels  $\delta = 0\%, 5\%, 7\%$ , with initial boundary  $\Gamma^0 = \partial B_{0.575}(0)$

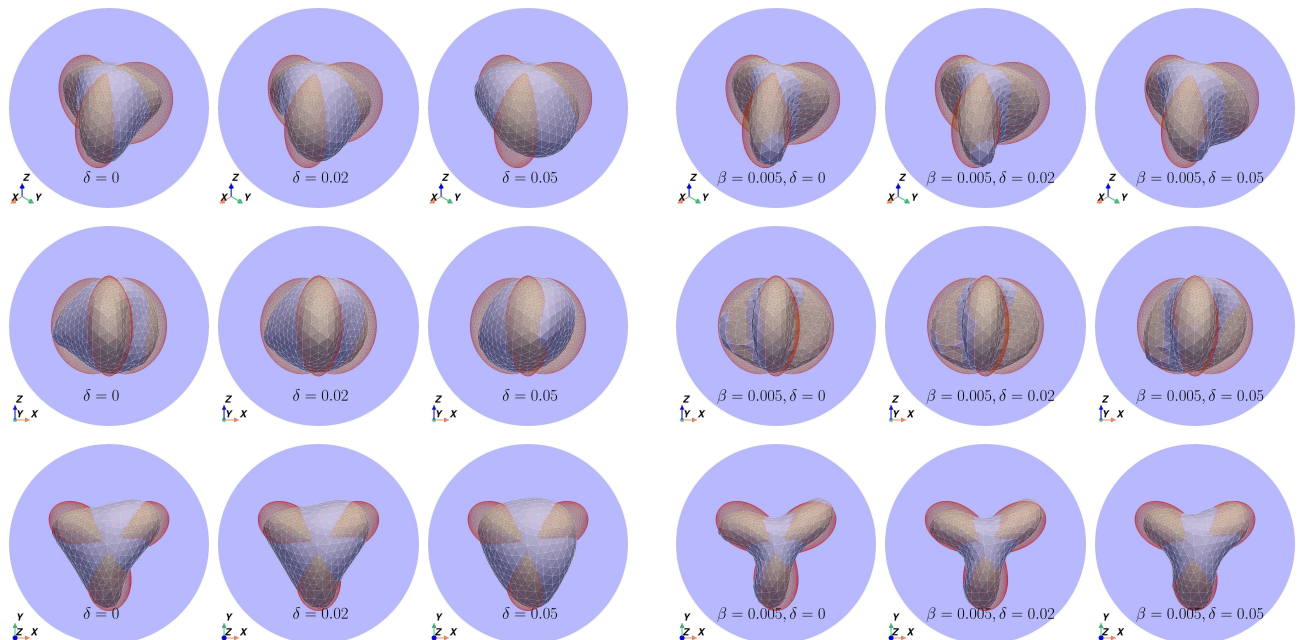


Figure 7: Reconstructed shapes using CCBM (left) and Algorithm 3 (right) under noise levels  $\delta = 0\%, 5\%, 7\%$ , with initial boundary  $\Gamma^0 = \partial B_{0.5}(0)$

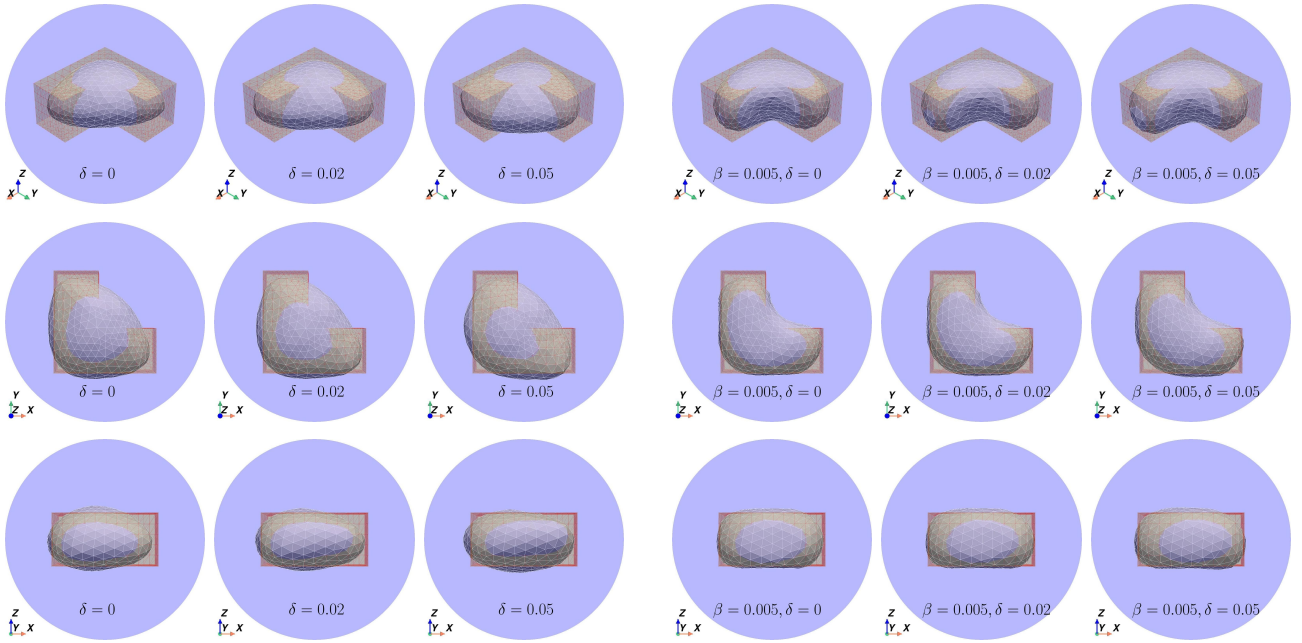


Figure 8: Reconstructed shapes using CCBM (left) and Algorithm 3 (right) under noise levels  $\delta = 0\%, 5\%, 7\%$ , with initial boundary  $\Gamma^0 = \partial B_{0.5}(0)$

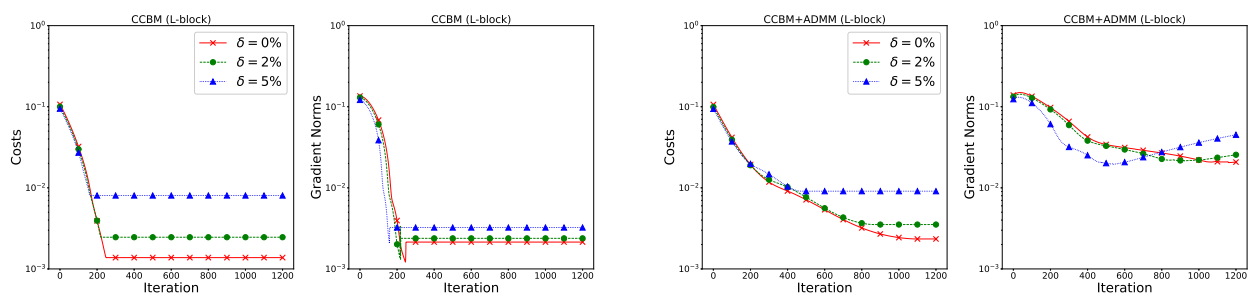


Figure 9: Histories of costs and gradient norms for the L-block case; left, conventional CCBM; right, proposed CCBM-ADMM scheme

## A Some useful identities

Let us write

$$\mathcal{M} = \mathcal{M}_1 + \mathcal{M}_2 := - \int_{\Omega} [\sigma A \nabla u \cdot \nabla \bar{p} + (\nabla \sigma \cdot \boldsymbol{\theta})(\nabla u \cdot \nabla \bar{p})] dx - \int_{\Omega} [C^T \mathbf{b} \cdot \nabla u \bar{p} + D \mathbf{b} \boldsymbol{\theta} \cdot \nabla u \bar{p}] dx.$$

Our main goal is to prove the last equation in (25). To do this, we first show that

$$\mathcal{M}_1 = - \int_{\Omega} \operatorname{div}(\sigma \nabla u)(\boldsymbol{\theta} \cdot \nabla \bar{p}) dx - \int_{\Omega} \operatorname{div}(\sigma \nabla \bar{p})(\boldsymbol{\theta} \cdot \nabla u) dx + \int_{\Gamma} \sigma \partial_{\mathbf{n}} \bar{p} \partial_{\mathbf{n}} u \theta_n ds, \quad (39)$$

$$\mathcal{M}_2 = \int_{\Omega} (\mathbf{b} \cdot \nabla u)(\boldsymbol{\theta} \cdot \nabla \bar{p}) dx - \int_{\Omega} (\mathbf{b} \cdot \nabla \bar{p})(\boldsymbol{\theta} \cdot \nabla u) dx - \int_{\Omega} \operatorname{div} \mathbf{b}(\boldsymbol{\theta} \cdot \nabla u) \bar{p} dx, \quad (40)$$

and then using the state and adjoint equations (5) and (20), we establish the last equation in (25).

We verify only (39), as (40) can be established by a similar argument. Using expression  $A$  in (17), we note that  $\mathcal{M}_1$  can be written as follows:

$$\mathcal{M}_1 = - \int_{\Omega} \sigma ((\operatorname{div} \boldsymbol{\theta}) \mathbf{I} - D \boldsymbol{\theta} - (D \boldsymbol{\theta})^T) \nabla u \cdot \nabla \bar{p} dx - \int_{\Omega} (\nabla \sigma \cdot \boldsymbol{\theta})(\nabla u \cdot \nabla \bar{p}) dx.$$

Let  $\mathbf{J} = (\boldsymbol{\theta} \cdot \nabla u)(\sigma \nabla \bar{p}) + (\boldsymbol{\theta} \cdot \nabla \bar{p})(\sigma \nabla u) - \sigma(\nabla u \cdot \nabla \bar{p})\boldsymbol{\theta}$ . Then,

$$\begin{aligned} \operatorname{div} \mathbf{J} &= (\boldsymbol{\theta} \cdot \nabla u) \operatorname{div}(\sigma \nabla \bar{p}) + (\boldsymbol{\theta} \cdot \nabla \bar{p}) \operatorname{div}(\sigma \nabla u) - (\nabla \sigma \cdot \boldsymbol{\theta})(\nabla u \cdot \nabla \bar{p}) \\ &\quad - \operatorname{div} \boldsymbol{\theta}(\sigma \nabla u \cdot \nabla \bar{p}) + \sigma \nabla \bar{p} \cdot \nabla(\boldsymbol{\theta} \cdot \nabla u) + \sigma \nabla u \cdot \nabla(\boldsymbol{\theta} \cdot \nabla \bar{p}) - \sigma \nabla(\nabla u \cdot \nabla \bar{p}) \cdot \boldsymbol{\theta}. \end{aligned} \quad (41)$$

The last three summands can be expressed as follows:

$$\left\{ \begin{array}{l} \mathbf{J}_1 := \sigma \nabla \bar{p} \cdot \nabla(\boldsymbol{\theta} \cdot \nabla u) = \nabla^2 u \boldsymbol{\theta} \cdot \sigma \nabla \bar{p} + \sigma D \boldsymbol{\theta}^T \nabla u \cdot \nabla \bar{p}, \\ \mathbf{J}_2 := \sigma \nabla u \cdot \nabla(\boldsymbol{\theta} \cdot \nabla \bar{p}) = \nabla^2 \bar{p} \boldsymbol{\theta} \cdot \sigma \nabla u + \sigma D \boldsymbol{\theta} \nabla u \cdot \nabla \bar{p}, \\ -\mathbf{J}_3 := \sigma \nabla(\nabla u \cdot \nabla \bar{p}) \cdot \boldsymbol{\theta} = \nabla^2 u \boldsymbol{\theta} \cdot \sigma \nabla \bar{p} + \nabla^2 \bar{p} \boldsymbol{\theta} \cdot \sigma \nabla u. \end{array} \right. \quad (42)$$

Hence,  $\mathbf{J}_1 + \mathbf{J}_2 + \mathbf{J}_3 = \sigma D \boldsymbol{\theta}^T \nabla u \cdot \nabla \bar{p} + \sigma D \boldsymbol{\theta} \nabla u \cdot \nabla \bar{p}$ . Substituting this into (41), rearranging, and integrating over  $\Omega$  yields

$$\mathcal{M}_1 = - \int_{\Omega} \operatorname{div}(\sigma \nabla \bar{p}) \boldsymbol{\theta} \cdot \nabla u dx - \int_{\Omega} \operatorname{div}(\sigma \nabla u) \boldsymbol{\theta} \cdot \nabla \bar{p} dx + \int_{\Omega} \operatorname{div} \mathbf{J} dx.$$

Applying the divergence theorem with  $\boldsymbol{\theta} = \mathbf{0}$  on  $\Sigma$ , and noting that for any function  $\varphi$  vanishing on  $\Gamma$  one has  $\nabla \varphi = \partial_{\mathbf{n}} \varphi \mathbf{n}$  on  $\Gamma$ , the last integral becomes  $\int_{\Omega} \operatorname{div} \mathbf{J} dx = \int_{\Gamma} \mathbf{J} \cdot \mathbf{n} ds = \int_{\Gamma} \sigma \partial_{\mathbf{n}} \bar{p} \partial_{\mathbf{n}} u \theta_n ds$ , which, after substituting back into the previous expression for  $\mathcal{M}_1$ , yields the desired form of  $\mathcal{M}_1$ .

From the previous computations,  $\mathcal{M}$  can be equivalently written as

$$\begin{aligned} \mathcal{M} &= \int_{\Omega} [-\operatorname{div}(\sigma \nabla u) + (\mathbf{b} \cdot \nabla u)] \boldsymbol{\theta} \cdot \nabla \bar{p} dx + \int_{\Gamma} \sigma \partial_{\mathbf{n}} \bar{p} \partial_{\mathbf{n}} u \theta_n ds \\ &\quad - \int_{\Omega} [\operatorname{div}(\sigma \nabla \bar{p}) + \mathbf{b} \cdot \nabla \bar{p} + \operatorname{div} \mathbf{b} \bar{p}] \boldsymbol{\theta} \cdot \nabla u dx =: R_1 + R_2 + R_3. \end{aligned}$$

By applying the state and adjoint equations (5) and (20), the volume integrals  $R_1$  and  $R_3$  reduce to  $R_1 = 0$  and  $R_3 = - \int_{\Omega} u_2(\boldsymbol{\theta} \cdot \nabla u) dx$ . Hence, we obtain  $\mathcal{M} = \int_{\Gamma} \sigma \partial_{\mathbf{n}} \bar{p} \partial_{\mathbf{n}} u \theta_n ds - \int_{\Omega} u_2(\boldsymbol{\theta} \cdot \nabla u) dx$ , which proves the last equation in (25).

## B Proof of Proposition 8

*Proof of Proposition 8.* Applying the chain rule together with the material derivative approach and the identity (22), we obtain the following expression for the shape derivative of  $Y^k(\Omega)$ :

$$\begin{aligned} dY^k(\Omega)[\boldsymbol{\theta}] &= \int_{\Omega} [u_2 \dot{u}_2 + (\beta(u_1 - v^k) + \lambda^k) \dot{u}_1] dx \\ &\quad - \int_{\Omega} [u_2 (\boldsymbol{\theta} \cdot \nabla u_2) + (\beta(u_1 - v^k) + \lambda^k) (\boldsymbol{\theta} \cdot \nabla u_1)] dx \\ &\quad + \int_{\Gamma} \left( \frac{\beta}{2} (v^k)^2 - \lambda^k v^k \right) \theta_n ds \\ &=: \Upsilon_1 - \Upsilon_2 + \Upsilon_3. \end{aligned} \tag{43}$$

To eliminate  $\dot{u}_1, \dot{u}_2$ , we use the adjoint system (34). Its variational formulation, upon taking complex conjugates of the equation, reads

$$-\int_{\Omega} (\sigma \nabla \bar{q} \cdot \nabla \varphi + (\mathbf{b} \cdot \nabla \varphi) \bar{q}) dx - i \int_{\Sigma} \bar{q} \varphi ds = \int_{\Omega} (-i(\beta(u_1 - v^k) + \lambda^k) - u_2) \varphi dx, \quad \forall \varphi \in \mathbf{V}(\Omega).$$

Setting  $\varphi = \dot{u}$  yields

$$a(\dot{u}, q) = \int_{\Omega} (i(\beta(u_1 - v^k) + \lambda^k) + u_2) \dot{u} dx. \tag{44}$$

On the other hand, from (18) with  $\psi = q$  and  $B = \operatorname{div}_{\tau} \boldsymbol{\theta} = 0$  on  $\Sigma$ , and using computations similar to Appendix A, we obtain

$$a(\dot{u}, q) = \mathcal{M}(u, q) = \int_{\Omega} (i(\beta(u_1 - v^k) + \lambda^k) + u_2) (\boldsymbol{\theta} \cdot \nabla u) dx + \int_{\Gamma} \sigma \partial_{\mathbf{n}} u \partial_{\mathbf{n}} \bar{q} \theta_n ds. \tag{45}$$

Comparing (44) and (45) gives

$$\int_{\Omega} (i(\beta(u_1 - v^k) + \lambda^k) + u_2) \dot{u} dx = \int_{\Omega} (i(\beta(u_1 - v^k) + \lambda^k) + u_2) (\boldsymbol{\theta} \cdot \nabla u) dx + \int_{\Gamma} \sigma \partial_{\mathbf{n}} u \partial_{\mathbf{n}} \bar{q} \theta_n ds.$$

Taking imaginary parts and rearranging yields:  $\Upsilon_1 - \Upsilon_2 = \int_{\Gamma} \sigma (\partial_{\mathbf{n}} q_1 \partial_{\mathbf{n}} u_2 - \partial_{\mathbf{n}} q_2 \partial_{\mathbf{n}} u_1) \theta_n ds$ . Substituting this into (43) gives the final expression (8), which completes the proof.  $\square$

## Acknowledgments

The work of JFTR is supported by the JSPS Postdoctoral Fellowships for Research in Japan (Grant Number JP24KF0221), and partially by the JSPS Grant-in-Aid for Early-Career Scientists (Grant Number JP23K13012) and the JST CREST (Grant Number JPMJCR2014).

## References

- [1] R. A. Adams and J. J. F. Fournier. *Sobolev Spaces*, volume 140 of *Pure and Applied Mathematics*. Academic Press, Amsterdam, 2003.
- [2] L. Afraites. A new coupled complex boundary method (CCBM) for an inverse obstacle problem. *Discrete Contin. Dyn. Syst. Ser. S*, 15(1):23 – 40, 2022.

- [3] L. Afraites, M. Dambrine, K. Eppler, and D. Kateb. Detecting perfectly insulated obstacles by shape optimization techniques of order two. *Discrete Contin. Dyn. Syst. Ser. B*, 8(2), 2007.
- [4] L. Afraites, M. Dambrine, and D. Kateb. Shape methods for the transmission problem with a single measurement. *Numer. Funct. Anal. Optim.*, 28(5–6):519–551, 2007.
- [5] L. Afraites, M. Dambrine, and D. Kateb. On second order shape optimization methods for electrical impedance tomography. *SIAM J. Control Optim.*, 47(3):1556–1590, 2008.
- [6] L. Afraites and J. F. T. Rabago. Boundary shape reconstruction with robin condition: existence result, stability analysis, and inversion via multiple measurements. *Comput. Appl. Math.*, 43:Art. 270, 2024.
- [7] M. Andrle and A. E. Badia. Identification of multiple moving pollution sources in surface waters or atmospheric media with boundary observations. *Inverse Problems*, 28:075009, 2002.
- [8] H. Azegami. *Shape Optimization Problems*, volume 164 of *Springer Optimization and Its Applications*. Springer, Singapore, 2020.
- [9] J. B. Bacani and G. H. Peichl. On the first-order shape derivative of the Kohn-Vogelius cost functional of the Bernoulli problem. *Abstr. Appl. Anal.*, 2013:19 pp. Article ID 384320, 2013.
- [10] A. E. Badia and T. H. Duong. On an inverse source problem for the heat equation. application to a pollution detection problem. *J. Inverse Ill-Posed Probl.*, 10:585–599, 2002.
- [11] A. E. Badia, T. H. Duong, and A. Hamdi. Identification of a point source in a linear advection-dispersion-reaction equation: application to a pollution source problem. *Inverse Problems*, 21:1121–1136, 2005.
- [12] A. Boulkhemair and A. Chakib. On the uniform Poincaré inequality. *Comm. Partial Differential Equations*, 32:1439–1447, 2007.
- [13] F. Caubet, M. Dambrine, and D. Kateb. Shape optimization methods for the inverse obstacle problem with generalized impedance boundary conditions. *Inverse Problems*, 29:Art. 115011 (26pp), 2013.
- [14] F. Caubet, M. Dambrine, D. Kateb, and C. Z. Timimoun. A Kohn-Vogelius formulation to detect an obstacle immersed in a fluid. *Inverse Prob. Imaging*, 7(1):123–157, 2013.
- [15] D. Choenais. On the existence of a solution in a domain identification problem. *J. Math. Anal. Appl.*, 52:189–219, 1975.
- [16] X. L. Cheng, R. F. Gong, W. Han, and X. Zheng. A novel coupled complex boundary method for solving inverse source problems. *Inverse Problems*, page Article 055002, 2014.
- [17] E. Cherrat, L. Afraites, and J. F. T. Rabago. Numerical solution by shape optimization method to an inverse shape problem in multi-dimensional advection-diffusion problem with space dependent coefficients. *Appl. Math. Optim.*, 92:Art. 13, 2025.

- [18] E. Cherrat, L. Afraites, and J. F. T. Rabago. Shape reconstruction for advection-diffusion problems by shape optimization techniques: The case of constant velocity. *Discrete Contin. Dyn. Syst. Ser. S*, 18(1):296–320, 2025.
- [19] M. Dambrine. On variations of the shape Hessian and sufficient conditions for the stability of critical shapes. *Rev. R. Acad. Cienc. Exactas Fis. Nat. Ser. A. Mat.*, 96:95–121, 2002.
- [20] M. Dambrine and M. Pierre. About stability of equilibrium shapes. *Model Math. Anal. Numer.*, 34:811–834, 2000.
- [21] R. Dautray and J.-L. Lions. *Mathematical Analysis and Numerical Methods for Science and Technology*, volume 3. Springer Science & Business Media, 1999.
- [22] M. C. Delfour and J.-P. Zolésio. Anatomy of the shape Hessian. *Annali di Matematica Pura ed Applicata*, 159(1):315–339, 1991.
- [23] M. C. Delfour and J.-P. Zolésio. *Shapes and Geometries: Metrics, Analysis, Differential Calculus, and Optimization*, volume 22 of *Adv. Des. Control*. SIAM, Philadelphia, 2nd edition, 2011.
- [24] S. Dempe. *Bilevel Optimization: Theory, Algorithms, Applications and a Bibliography*, volume 161 of *Springer Optimization and Its Applications*, pages 581–672. Springer International Publishing, 2020.
- [25] G. Doğan, P. Morin, R.H. Nochetto, and M. Verani. Discrete gradient flows for shape optimization and applications. *Comput. Methods Appl. Mech. Engrg.*, 196:3898–3914, 2007.
- [26] K. Eppler. Second derivatives and sufficient optimality conditions for shape functionals. *Control Cybernet.*, 29:485–512, 2000.
- [27] K. Eppler and H. Harbrecht. A regularized Newton method in electrical impedance tomography using shape hessian information. *Control Cybern.*, 34:203–225, 2005.
- [28] K. Eppler and H. Harbrecht. Shape optimization for free boundary problems – analysis and numerics. In G. Leugering, S. Engell, A. Griewank, M. Hinze, R. Rannacher, V. Schulz, M. Ulbrich, and S. Ulbrich, editors, *Constrained Optimization and Optimal Control for Partial Differential Equations*, volume 160 of *International Series of Numerical Mathematics*, pages 277–288, Basel, 2012. Springer.
- [29] L. Fernandez, A. A. Novotny, R. Prakash, and J. Sokołowski. Pollution sources reconstruction based on the topological derivative method. *Appl. Math. Optim.*, 84:1493–1525, 2021.
- [30] R. Gong, X. Cheng, and W. Han. A coupled complex boundary method for an inverse conductivity problem with one measurement. *Appl. Anal.*, 96(5):869–885, 2017.
- [31] A. Hamdi. Inverse source problem in a 2d linear evolution transport equation: detection of pollution source. *Inverse Probl. Sci. Eng.*, 20:401–421, 2012.
- [32] A. Hamdi and I. Mahfoudhi. Inverse source problem in a one-dimensional evolution linear transport equation with spatially varying coefficients: application to surface water pollution. *Inverse Probl. Sci. Eng.*, 21:1007–1031, 2012.

- [33] H. Harbrecht and J. Tausch. An efficient numerical method for a shape-identification problem arising from the heat equation. *Inverse Problems*, 27(6):065013, 2011.
- [34] H. Harbrecht and J. Tausch. On the numerical solution of a shape optimization problem for the heat equation. *SIAM J. Sci. Comput.*, 35(1):A104–A121, 2013.
- [35] J. Haslinger, K. Ito, T. Kozubek, K. Kunisch, and G. H. Peichl. On the shape derivative for problems of Bernoulli type. *Interfaces Free Bound.*, 11:317–330, 2009.
- [36] F. Hecht. New development in FreeFem++. *J. Numer. Math.*, 20:251–265, 2012.
- [37] A. Henrot and M. Pierre. *Shape Variation and Optimization: A Geometrical Analysis*, volume 28 of *Tracts in Mathematics*. European Mathematical Society, Zürich, 2018.
- [38] R. Kohn and M. Vogelius. Relaxation of a variational method for impedance computed tomography. *Commun. Pure Appl. Math.*, 40(6):745–777, 1987.
- [39] R. Kress and D. Colton. *Inverse Acoustic and Electromagnetic Scattering Theory*, volume 93 of *Applied Mathematical Sciences*. Springer, New York, 3rd edition, 1998.
- [40] F. Murat and J. Simon. Sur le contrôle par un domaine géométrique. Research report 76015, Univ. Pierre et Marie Curie, Paris, 1976.
- [41] S. Neelz. Limitations of an analytical solution for advection-diffusion with variable coefficients. *Commun. Numer. Methods Eng.*, 22:387–396, 2006.
- [42] J. W. Neuberger. *Sobolev Gradients and Differential Equations*. Springer-Verlag, Berlin, 1997.
- [43] A. Okubo. *Diffusion and Ecological Problems: Mathematical Models*. Springer, New York, NY, 1980.
- [44] H. Ouaissa, A. Chakib, A. Nachaoui, and M. Nachaoui. On numerical approaches for solving an inverse Cauchy Stokes problem. *Appl. Math. Optim.*, 85(Art. 3):37 pp., 2022.
- [45] J. F. T. Rabago. On the new coupled complex boundary method in shape optimization framework for solving stationary free boundary problems. *Math. Control Relat. Fields*, 13(4):1362–1398, 2023.
- [46] J. F. T. Rabago. Localization of tumor through a non-conventional numerical shape optimization technique. *Appl. Numer. Math.*, 217:135–171, 2025.
- [47] J. F. T. Rabago, L. Afraites, and H. Notsu. Detecting immersed obstacle in Stokes fluid flow using the coupled complex boundary method. *SIAM J. Control & Optim.*, 63(2):822–851, 2025.
- [48] J. F. T. Rabago and H. Azegami. Shape optimization approach to defect-shape identification with convective boundary condition via partial boundary measurement. *Japan J. Indust. Appl. Math.*, 31(1):131–176, 2018.
- [49] J. F. T. Rabago and H. Azegami. A second-order shape optimization algorithm for solving the exterior Bernoulli free boundary problem using a new boundary cost functional. *Comput. Optim. Appl.*, 77(1):251–305, 2020.

- [50] J. F. T. Rabago, A. Hadri, L. Afraites, A. S. Hendy, and M. A. Zaky. A robust alternating direction numerical scheme in a shape optimization setting for solving geometric inverse problems. *Comput. Math. Appl.*, 175:19–32, September 2024.
- [51] J. F. T. Rabago and H. Notsu. Numerical solution to a free boundary problem for the Stokes equation using the coupled complex boundary method in shape optimization setting. *Appl. Math. Optim.*, 89:Art. 2, 2024.
- [52] J. Simon. Differentiation with respect to the domain in boundary value problems. *Numer. Funct. Anal. Optim.*, 2:649–687, 1980.
- [53] J. Sokółowski and J.-P. Zolésio. *Introduction to Shape Optimization: Shape Sensitivity Analysis*. Springer Series in Computational Mathematics. Springer-Verlag, Berlin, Heidelberg, 1992.
- [54] W. Yan, J. Hou, and Z. Gao. Shape identification for convection-diffusion problem based on the continuous adjoint method. *Appl. Math. Lett.*, 64:74–80, 2017.
- [55] W. Yan, J. Su, and F. Jing. Shape reconstruction for unsteady advection-diffusion problems by domain derivative method. *Abstr. Appl. Anal.*, 2014(Art. ID 673108):7 pp., 2014.
- [56] X. Zheng, X. Cheng, and R. Gong. A coupled complex boundary method for parameter identification in elliptic problems. *Int. J. Comput. Math.*, 97(5):998–1015, 2020.
- [57] C. Zoppou and J. H. Knight. Analytical solution of a spatially variable coefficient advection-diffusion equation in up to three dimensions. *Appl. Math. Model.*, 23(9):667–685, 1999.